

# 1 **CloudViT: exploring cloud type classification with vision transformers**

## 2 **in global satellite data.**

3

4 Julien Lenhardt <sup>1</sup>, Johannes Quaas <sup>1,2</sup>, Dino Sejdinovic <sup>3</sup>, Daniel Klocke <sup>4</sup>

5

6 <sup>1</sup>Leipzig Institute for Meteorology, Universität Leipzig, Leipzig, Germany

7 <sup>2</sup>ScaDS.AI - Center for Scalable Data Analytics and Artificial Intelligence, Leipzig University, Humboldtstraße 25, 04105

8 Leipzig, Germany

9 <sup>3</sup>School of Computer and Mathematical Sciences & Australian Institute for Machine Learning, University of Adelaide, Adelaide,

10 Australia

11 <sup>4</sup>Max Planck Institute for Meteorology (MPI-M), Hamburg, Germany

12 *Correspondence to:* Julien Lenhardt (julien.lenhardt@uni-leipzig.de)

### 13 Abstract

14

15 Clouds constitute, through their interactions with incoming solar radiation and outgoing terrestrial radiation, a fundamental  
16 element of the Earth's climate system. Different cloud types show a variety in cloud microphysical or optical properties, phase,  
17 or vertical extent, and thus disparate radiative effects. Both in observational and model datasets, classifying clouds is important  
18 since different cloud types respond differently to current and future anthropogenic climate change. Cloud types have traditionally  
19 been defined using a simplified partition of cloud top pressure and optical thickness, but recently using deep learning. In this  
20 study, we present a method called CloudViT (Cloud Vision Transformer) building on surface observations and spatial extracts of  
21 cloud properties from the MODIS instrument to derive cloud types, leveraging spatial patterns with a vision transformer model.  
22 The performance of the model is fair and hampered by the limited number of samples and the challenging matching between data  
23 sources arising during the collocation process. The method is then evaluated through the distributions of cloud type properties and  
24 global spatial patterns of cloud type occurrences. Potential improvements emerge in the reduction in mismatches between data  
25 sources, the extension of the colocated dataset, and the refinement of the classification model. While the application of the  
26 method in its current state comes with apparent uncertainties due to limited performance, it raises relevant challenges and  
27 limitations, from which the community can benefit from discussing for the development of similar methods. To foster future  
28 advancements, the dataset and model are available from Zenodo (Lenhardt et al., 2024b).

29

## 30 1 Introduction

31

32 Clouds form an essential component in the Earth's climate, by impacting the atmospheric energy budget and water cycle, and by  
33 influencing the reflected solar radiation as well as the outgoing terrestrial radiation fluxes. Clouds are highly variable spatially  
34 and temporally, and occur in a large variety of types (Howard, 1803; WMO, 2017). Typically, separating clouds between low and  
35 high (WMO, 1975), and between stratiform and cumuliform (WMO, 1975, 2017), reveals different and complex cloud effects on  
36 processes such as radiation and precipitation formation (Hartmann et al., 1992; Dhuria and Kyle, 1990). The high variability and  
37 complexity of clouds are some of the causes for the uncertainties in estimates of their response to anthropogenic climate change  
38 both currently and in the future (Boucher et al., 2013; Forster et al., 2021). These uncertainties manifest both in observational  
39 datasets for which the aim is to constrain past and current effects, and in climate models where cloud representation is of utmost  
40 importance to properly constrain future scenarios. Through the phase (liquid, ice or mixed), the droplet size distribution, the  
41 vertical structure or other micro- and macro-physical properties, different cloud types can lead to drastically diverse radiative  
42 effects making the cloud type a property of interest to help describe their involvement in the weather and climate system  
43 (Ramanathan et al., 1989; Slingo, 1990; Oreopoulos et al., 2017; Luo et al., 2023). Unravelling and understanding trends in  
44 clouds has become more tractable in recent decades due to the large amount of remote sensing data made available globally on a  
45 daily basis. However, analysing such extensive datasets manually becomes challenging, especially with the goal of extracting  
46 meaningful information about different cloud types based on their patterns, microphysical properties or radiative effects.  
47 Algorithms have taken over this complex task but still struggle to provide objective groupings out of the intricate spatio-temporal  
48 patterns observed in remote sensing data. At the same time, applying methods which are engineered on remote sensing data to  
49 climate models could become more viable as new global climate models are bridging the gap in resolution by reaching km-scale  
50 resolutions, though this transfer to climate model data comes with its own challenges.

51 Traditional cloud classification methods are built on simple characteristics. The standard classification developed as part of the  
52 International Satellite Cloud Climatology Project (ISCCP) relies on three levels (low, medium, high) of cloud altitude using as  
53 proxy the cloud top pressure (CTP) and three thresholds of cloud optical thickness (COT), defining overall nine cloud types  
54 (Rossow et al., 1991). This classification is performed on scalar fields, setting aside any spatial pattern in the cloud field from  
55 which information could be obtained to better inform the classification process. Relying on the same type of two-dimensional  
56 histograms, recent methods have been developed aiming at refining the created clusters and partially relaxing the constraints on  
57 the pre-defined thresholds (Tzallas et al., 2022). The reason to choose the two parameters is that such a classification lends itself  
58 to the analysis of cloud radiative effects: the cloud radiative effect in the solar is a monotonic function of COT, the one in the  
59 terrestrial spectrum, of CTP. However, one might be interested in sensitivities of cloud thickness or water content to different  
60 drivers (e.g., aerosols) for given cloud types, which is hampered by using CTP and COT to define the types. Also, COT does not  
61 map well onto the distinction between cumuliform and stratiform clouds. For such reasons, Unglaub et al. (2020) defined cloud  
62 regimes from cloud base height and variability in cloud top height, hinting at the added value of some measure of spatial  
63 variability and pattern. However, to leverage spatial structure and textures, cloud classification methods based on artificial  
64 intelligence (AI) have opened new avenues of research built upon vast amounts of remote sensing data. For example, using  
65 convolutional neural networks (CNNs; LeCun et al., 1989; LeCun et al., 1995), Zhang et al. (2018) use ground-based images and  
66 human-labelled cloud types to develop a model for meteorological cloud classification and support weather prediction tasks.  
67 Using a similar architecture, Rasp et al. (2020) classify clouds from expert-labelled satellite images of four different cloud  
68 organisation patterns in the trades. This method further emphasises how expert knowledge to identify cloud patterns can be  
69 learned by CNN models and allow to then better constrain radiative effects of mesoscale convection (Wood and Hartmann, 2006;  
70 Bony et al., 2020; Stevens et al., 2020) which would prove to be too cumbersome manually. The application of deep learning to  
71 the classification of mesoscale cloud patterns in particular (Muhlbauer et al., 2014; Yuan et al. 2020; McCoy et al., 2023)  
72 additionally demonstrates how specific cloud organization patterns, observable by experts in satellite data, can be learned by  
73 machine learning models, and allows a deeper analysis of their radiative effects and characteristics on longer time periods and  
74 larger spatial scales. These studies rely on human observers to initially classify clouds or cloud patterns directly from images,  
75 relying on visual aspects to distinguish clouds, and subsequently linking the identified cloud types to local meteorological  
76 conditions. Kuma et al. (2023) also capitalize on ground-based observations but connect them to shortwave and longwave  
77 radiation satellite retrievals at coarser spatial and temporal resolutions. The method relies on identifying patterns directly in  
78 radiation retrievals to associate them to daily occurrence probabilities of cloud types. This method has the benefit of being able to  
79 be used on outputs from large ensembles of global model simulations and reanalysis datasets which cover extended time-scales  
80 compared to observational datasets. Relying on similar model architectures, Zantedeschi et al. (2019) and Kaps et al. (2023)  
81 classify cloud types derived from active remote sensing labels. The study from Kaps et al. (2023) capitalizes on the model from

82 Zantedeschi et al. (2019) to extrapolate cloud type estimates using global passive remote sensing data, and jointly trains a model  
83 on coarsened data with spatial resolution similar to current global climate models. Other methods have been developed without  
84 the use of cloud type labels, drawing conclusions from clusters appearing in large remote sensing radiation retrievals (Kurihana  
85 et al., 2022). In general, the developed methods rely on identifying characteristic patterns arising in images (related to visible  
86 features of cloud types), radiation retrievals (related to radiative properties of cloud types), or cloud properties retrievals (related  
87 to physical properties of cloud types). Each choice of cloud type labels introduces a certain level of subjectivity in the derived  
88 cloud types. For example, there is less subjectivity in the expert-labelled images than in the produced cloud clusters, which  
89 naturally introduces some subsequent biases. Choosing certain input quantities also physically constrains the variability of cloud  
90 type properties which can hinder the interpretation of the derived cloud type estimates. However, the transferability to global  
91 climate model outputs is a great advantage of some of these methods as they provide a crucial way to diagnose the representation  
92 of clouds in climate models and push towards reducing uncertainties in representing future-climate clouds (Kuma et al. 2023;  
93 Kaps et al. 2023).

94 In this study, we investigate the classification of clouds by merging surface observations of cloud types and passive satellite  
95 retrievals of cloud properties, building a method called CloudViT (Cloud Vision Transformer). Following a similar methodology  
96 from previous work (Lenhardt et al., 2024a), we define cloud scenes as tiles of 128x128 pixels which encompass cloud  
97 microphysical and optical properties at a 1 km horizontal resolution. The employed cloud properties are from the MODerate  
98 Resolution Imaging Spectroradiometer (MODIS, Platnick et al. (2017)), and more particularly the cloud top height (CTH), the  
99 cloud optical thickness (COT) and the cloud water path (CWP), which are paired with surface network observations of cloud  
100 types (cf. Table 1). To harness the spatial aspect of the cloud scene and extract relevant features from the input cloud properties,  
101 we resort to computer vision models based on CNNs and transformers (Dosovitskiy et al., 2020). Firstly, a vision transformer  
102 model is trained in a self-supervised setting to create a condensed latent representation of the input cloud field. Subsequently, a  
103 simpler classification model is fitted to predict the cloud type corresponding to the cloud scene, learning from the labels of a  
104 wide ground-based observation network. The formulated method has the goal to produce estimates of cloud types while  
105 generalising from the local ground observations to global distributions, increasing both the temporal and spatial coverage. The  
106 method relies partly on the assumption that the observed cloud types exist on scales similar to the extent of the tiles, and  
107 additionally builds on the spatial patterns characteristic of different cloud types. Moreover, as the ground-based cloud type  
108 observations provide consistent labels which are only available at sparse locations, we can leverage long-standing instruments  
109 like MODIS to design an algorithm based on satellite retrievals suited to generalisation to global distributions.

110 Firstly, we introduce in section 2 the different datasets used in the study alongside the collocation process between the  
111 ground-based and satellite datasets. Subsequently, the different components of the CloudViT method are presented in section 3,  
112 supported by sensitivity studies about the generalisation skill of the models and the benefits of the spatial context. In section 4,  
113 we evaluate the method and investigate the distribution of cloud properties following the predicted cloud types. The results in  
114 section 5 focus on the extension to a global distribution of cloud types. Challenges, limitations, and lessons learned from  
115 CloudViT’s development are highlighted in the following section 6, with the guiding idea of making cloud type classification  
116 with vision transformers reliable, capable of achieving notable performance, and potentially applicable to high-resolution climate  
117 model simulations. Eventually, we conclude over the presented method and challenges of cloud type classification.

## 118 **2 Data**

119

### 120 **2.1 Surface observations**

121

122 The cloud type observations used in this study come from two similar global observation datasets maintained by the UK Met  
123 Office, one providing observations made at sea (Met Office, 2006) and the second providing observations made on land (Met  
124 Office, 2008). These observations are performed from weather stations (land or sea) or ships, by trained observers following the  
125 WMO code tables (WMO, 2019). Each cloud level (high, WMO code table 0509; medium, WMO code table 0515; low, WMO  
126 code table 0513; see Table A.1) is separated in 9 different types describing in more detail the aspect and type of the observed  
127 clouds. The labels thus provide a high level of detail regarding the observed cloud scene from the surface. Naturally, the case of  
128 multilayer clouds poses a problem since the field of view and the visibility from the surface are limited, which is why we remove  
129 the potential multilayered cases from the training dataset to focus only on single-layer observed cloud scenes. It induces potential  
130 selection bias issues as some cloud types might more likely be observed in multilayered configurations. The relative amounts of  
131 each cloud type before and after the filtering and collocation process are displayed in Figure 2. Similarly, uncertainty is greater for  
132 medium and high clouds as their observation can be more challenging than for low clouds. Furthermore, the spatial distribution

133 of the labels (Fig. 1, Fig. A.1) can be problematic as the marine observations are distributed mainly along ship routes. On the  
134 other hand, combining that with land observations provides a more complete representation of cloud types, especially for high  
135 level ones, all the while introducing the influence of orography. Other studies like Kuma et al. (2023) and Lenhardt et al. (2024a)  
136 have built estimates of cloud quantities based on these ground-based observation datasets, overcoming limitations pertaining to  
137 incomplete field of view and disparate spatial distribution.

138 For simplifying the analysis but also the training of the classification model, we group the 27 reported WMO cloud types into 4  
139 and 10 categories, similarly to Kuma et al. (2023). The first categorisation allows for broad classification by dividing the cloud  
140 species into high, medium, cumuliform and stratiform types. The second categorisation provides a more detailed classification  
141 while still limiting the subdivision of similar cloud types. This prevents a too pronounced unbalance in the cloud type labels  
142 while possibly removing some of the subjective biases and uncertainty stemming from the human observers. The detailed  
143 categories corresponding to the WMO codes are available in Table A.1 and shown in Figure 2.

144

## 145 **2.2 Satellite retrievals**

146

147 In addition to the surface observations, we use satellite retrievals from MODIS, in particular from the AQUA satellite. MODIS  
148 retrievals offer a vast amount of data at kilometre-scale resolution with daily overpasses. Each of the supplied granule file  
149 contains cloud microphysical and optical properties across a region with a span of around 2330 km x 2000 km. We make use of  
150 the available CUMULO dataset (Zantedeschi et al., 2019) since it allows access to preprocessed MODIS level 2 satellite data,  
151 with global coverage, and for two full years (2008 and 2016). Among the data variables available, we rely on two unified  
152 products (cf. Table 1) describing either cloud properties (MODIS06 level 2 cloud product, hereafter MYD06; Platnick et al.,  
153 2017) or the cloud cover (MODIS35 level 2 cloud flag mask, hereafter MYD35; Ackerman et al., 2017). The latter's main usage  
154 is to help screen for cloud scenes with a minimum cloud coverage.

155 The MYD06 data product incorporates miscellaneous properties pertaining to the cloud top (temperature, pressure, height)  
156 alongside some microphysical and optical properties (effective radius, water path, optical depth). As mentioned previously, our  
157 method builds upon level 2 data which are typically obtained from calibrated radiances through methods described in Platnick et  
158 al. (2017). More specifically, cloud top properties are retrieved using several radiance channels: harnessing the opacity of CO<sub>2</sub>,  
159 the CTP of high clouds is retrieved with wavelengths in the CO<sub>2</sub> absorption range, while infrared wavelengths combined with  
160 simulated brightness temperatures are used for lower and thicker clouds. The related CTH retrieval can thus suffer from regional  
161 biases as the brightness temperatures are based on vertical profiles from reanalysis using regional and monthly averaged lapse  
162 rate data along with surface temperature (Baum et al., 2012). The method introduced here can thus incorporate said biases from  
163 the input data into the learning process. The microphysical and optical properties of clouds - COT and cloud effective radius  
164 (CER) - are retrieved concurrently from multispectral reflectances, CTP values, surface types and cloud masks. Lastly, the CWP  
165 is also retrieved as part of the cloud optical properties algorithm detailed in Platnick et al. (2017). The additional input quantities  
166 needed to derive and retrieve the mentioned cloud properties (e.g. water vapour and ozone vertical profiles from reanalysis;  
167 Platnick et al., 2003; Baum et al., 2012) can result in subsequent uncertainties where only sparse observations like in remote  
168 marine areas are available for the data assimilation. Eventually, from the entirety of available MYD06 retrievals, we select three  
169 cloud properties in particular, namely the CTH, COT, and CWP.

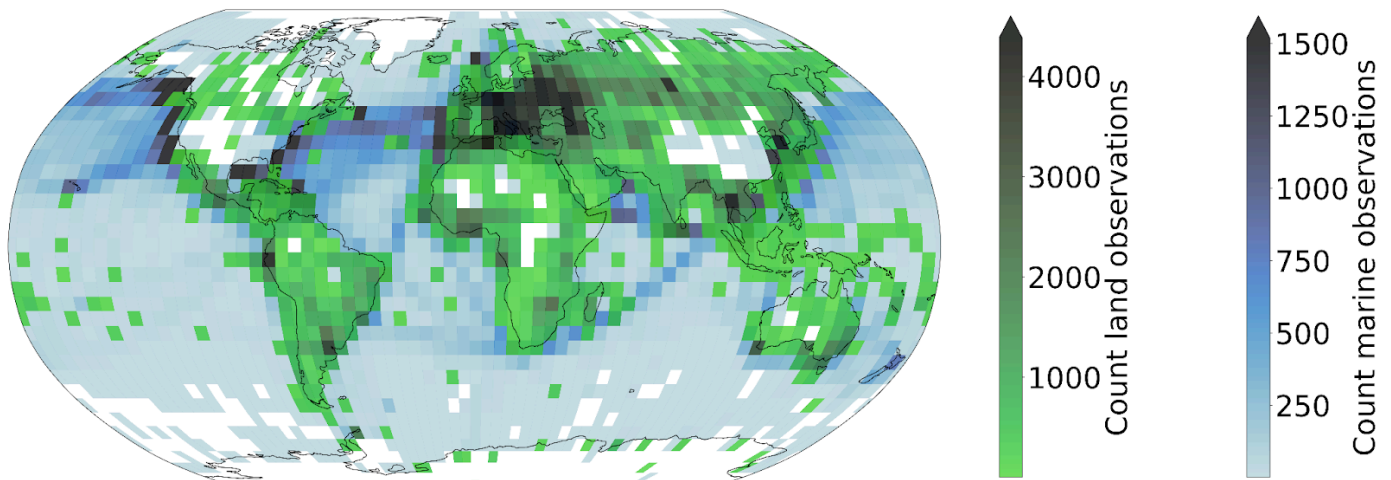
170 As a whole, the MYD06 product has the advantage that, building directly on cloud properties, we can design a classification  
171 model from which the relationship between cloud type and other cloud properties can then be examined. Relying on calibrated  
172 radiances which lie ahead in the retrieval process could offer a more neutral input but due to the large associated dimensionality,  
173 extracting information about clouds might become more challenging. Additionally, basing the method on commonly used cloud  
174 properties allows us to directly associate the results with other derived cloud classifications, making the comparison and  
175 understanding of the predictions more straightforward. Nevertheless, the biases introduced by using level 2 data in comparison to  
176 level 1 calibrated radiances and reflectances should be properly characterised and taken into account in the behaviour of the  
177 statistical model.

178 Alongside the colocated dataset, we build a collection of randomly sampled tiles out of the satellite retrievals from the year 2008.  
179 For each granule, a maximum of 20 tiles are sampled while ensuring the amount of missing data stays limited. This process leads  
180 to the compilation of more than 1.3M single tiles of cloud properties. These tiles are then randomly split temporally into training  
181 (70%), validation (10%) and test (20%) sets. This dataset is the basis for the self-supervised training procedure presented in the  
182 following section.

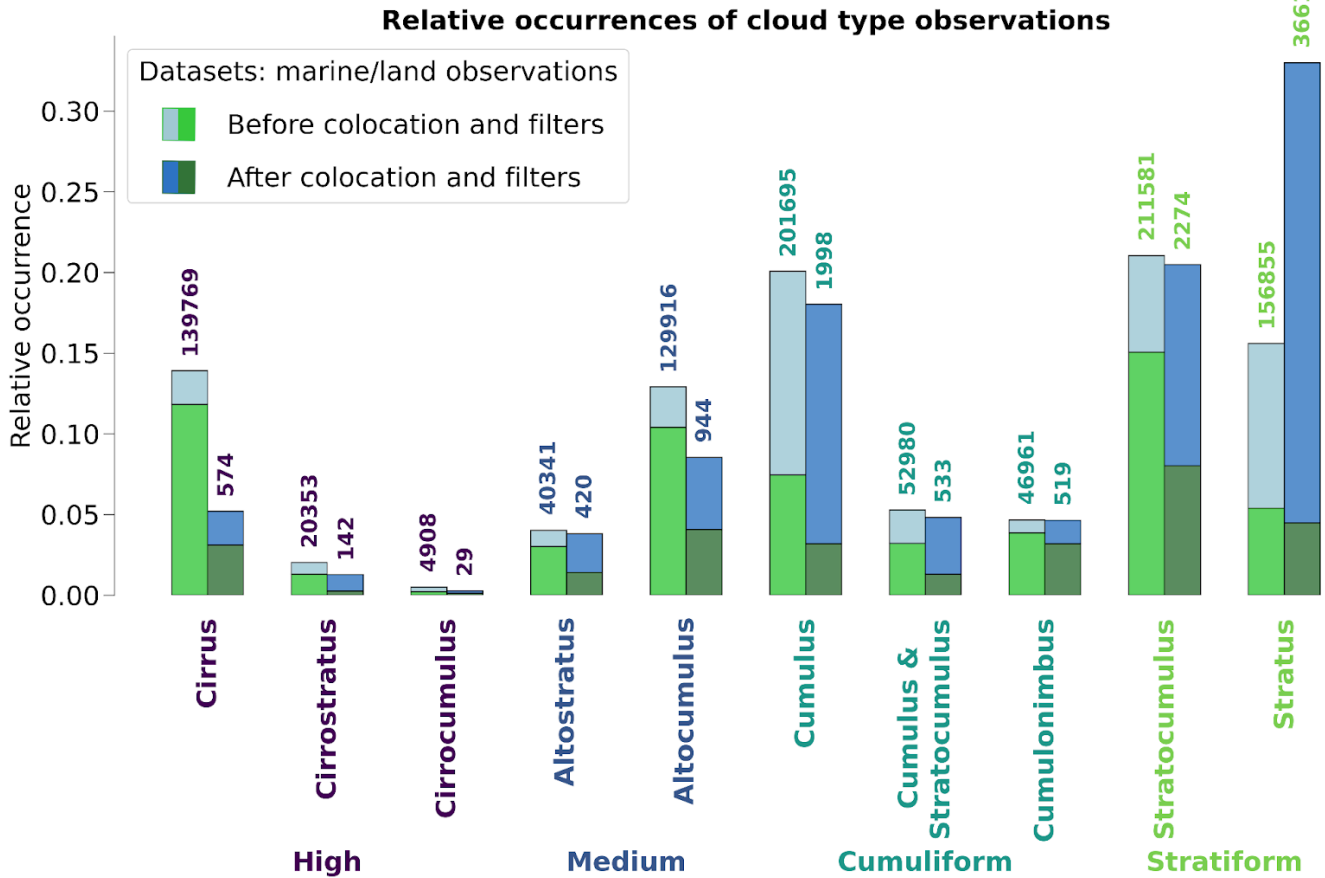
Data product	Description	Variables	Resolution	Usage
Global marine meteorological observations (Met Office, 2006)	Marine surface observations	Cloud type	Latitude/longitude coordinates 0.1° Hourly/daily observations	Labels
Land SYNOP reports (Met Office, 2008)	Land surface observations	Cloud type	Latitude/longitude coordinates 0.1° Hourly/daily observations	Labels
MODIS Atmosphere L2 Cloud Product (MYD06) (Platnick, 2017)	Cloud-top properties, cloud optical and microphysical properties	Cloud top height, CTH (m) Cloud optical thickness, COT (a.u.) Cloud water path, CWP (g.m <sup>-2</sup> )	1-km pixel resolution Daily overpass	Input features
MODIS Atmosphere L2 Cloud Mask Product (MYD35) (Ackerman, 2017)	Cloud pixel flag	Cloud mask	1-km resolution Daily overpass	Used for cloud scene filtering

184 **Table 1 : Datasets description. The surface observations are provided by a worldwide station network available from the**  
 185 **UK MetOffice (Met Office, 2006; Met Office, 2008; see section 2.1). The MODIS data are derived from the collection 6.1**  
 186 **of the datasets (Ackerman, 2017; Platnick et al., 2017; see section 2.2).**  
 187

### Marine (2008, 2016) & land (2016) cloud type observations count



188 **Figure 1: Spatial distribution of cloud type observations for marine (years 2008 and 2016; Met Office, 2006) and land**  
 189 **(year 2016; Met Office, 2008). The corresponding spatial distributions of cloud type observations are included in Figures**  
 190 **A.1 and A.2, for before and after the colocation process, respectively.**  
 191  
 192



193

194 **Figure 2: Relative occurrences of cloud types before and after the collocation and filtering process, indicated for both the**  
 195 **marine (blue; Met Office, 2006) and land (green; Met Office, 2008) observational datasets. The x axis corresponds to the**  
 196 **cloud types in the case of 4 and 10 categories. The corresponding numbers of collocated samples for each cloud type are**  
 197 **detailed in Table A.1.**

### 198 3 Method

199

#### 200 3.1 Method outline

201

202 Relying on computer vision models and their large number of trainable parameters usually requires adapting the training strategy,  
 203 particularly when the training dataset is of modest size. In the presented study, the amount of labels available is greatly reduced  
 204 during the collocation process (see Table A.1 for the number of samples per cloud type) but still contains useful and exploitable  
 205 information about the observed cloud types. We thus introduce a self-supervised learning process which allows us to draw on the  
 206 larger amount of satellite data available before addressing the more complex task of cloud classification. The larger purpose of  
 207 this methodology is to be able to classify clouds on a global scale, outside of the areas where surface observations were made and  
 208 outside of the typical coverage of human observation stations.

209 For the self-supervised task, we train two models to reconstruct 3D data cubes of cloud properties. The first model, which is used  
 210 as a baseline, is a CNN backbone we previously presented in Lenhardt et al. (2024a) to handle satellite retrievals of cloud  
 211 properties for cloud base height prediction. The second model we develop in this study is based on vision transformers  
 212 (Dosovitskiy et al., 2020), a recent type of model compared to the more typical CNNs for computer vision applications. The  
 213 spatial pattern of the cloud properties and their scale provide information about clouds, which can be leveraged to classify them  
 214 for example into more stratiform and more cumuliform types. During the training phase of these models, the samples are images  
 215 of size 128x128 pixels consisting of three different cloud properties: CTH, COT and CWP. We ensure that the models learn to  
 216 distinguish cloud patterns and not to recognise specific geographical locations by extracting samples randomly across global  
 217 satellite retrievals from the year 2008, without adding information about their location. In a second step, a classification model is  
 218 trained on the collocated samples of cloud properties and surface observations. As mentioned in section 2.1, the number of types

219 reported in the observations for clouds is reduced to either 4 or 10 classes (Kuma et al. 2023). The training process follows a  
 220 supervised learning framework, where the classification model outputs a single cloud type (among the 4 or 10 cloud types) for  
 221 the whole extent of the input cloud scene of size 128x128 pixels. The benefit of the presented method using either a CNN or a  
 222 vision transformer, which are models incorporating a certain level of spatial awareness, is that it is consistent with the cloud type  
 223 identified by the human observer. Furthermore, in comparison to conventional methods like the ISCCP, the method benefits from  
 224 a potential ability to distinguish cloud types without using predefined thresholds.

225

### 226 3.2 Vision transformer

227

228 Vision transformers were introduced by Dosovitskiy et al. (2020), building on the transformer architecture previously presented  
 229 in Vaswani et al. (2017) which was mainly applied to natural language processing (NLP) tasks. The adaptation to images was  
 230 made by splitting images into patches of a certain size, 16 pixels in the case of the seminal paper, and providing the sequence of  
 231 embeddings of these patches to a transformer. The patches from the images are then treated as words would be in a NLP  
 232 application. The transformer can then be trained in a supervised fashion to classify the input images. They have been shown to  
 233 perform at the same level or even outperform classical computer vision models like ResNets on tasks like classification (e.g. see  
 234 Section 4 of Dosovitskiy et al., 2020). However, as mentioned in section 3.1, this type of model, alongside CNNs, is data hungry  
 235 and requires a large number of labelled samples to be trained from scratch in a supervised fashion. In this setting, self-supervised  
 236 pretraining can lead to highly performant models while not requiring a larger training dataset. We train a vision transformer  
 237 following the self-supervised pretraining methodology presented in Atito et al. (2023), named Self-supervised vision  
 238 Transformer (SiT). This methodology allows to train vision transformers in a self-supervised fashion building on the concept of  
 239 Group Masked Model Learning (GMML), additionally using the same autoencoder framework as with traditional CNNs like the  
 240 commonly used U-Net (Ronneberger et al., 2015) or our baseline model from Lenhardt et al. (2024a). The SiT architecture used  
 241 in this study is adapted from the seminal vision transformer architecture (Dosovitskiy et al., 2020) by setting the latent dimension  
 242 to 256, similarly to the CNN architecture introduced in Lenhardt et al. (2024a).

243 One strength of the transformer architecture is the possibility to easily include several simultaneous learning tasks. We can use  
 244 this ability to our advantage and incorporate two objectives for the self-supervised training process: input reconstruction  
 245 following GMML and contrastive learning. The input reconstruction is achieved by adapting the transformer into an autoencoder  
 246 architecture. Like with traditional CNN autoencoders, the task is for the model to reconstruct the provided input. We benefit  
 247 further from another advantage of vision transformers as they showcase a reduced complexity compared to CNNs since they rely  
 248 to a much lesser degree on convolution operations. The methodology of Atito et al. (2023) additionally uses recent results in  
 249 GMML to further help in the self-supervised learning task. The framework of GMML is integrated in the reconstruction task by  
 250 replacing random parts of the input image with noise. The overarching goal of this image modification is to train the model to  
 251 learn semantic representations of the input data, allowing reconstruction of masked areas only with knowledge of some other  
 252 patches in the input image. The objective for this reconstruction task hence takes the form of the l1-loss, a commonly used metric  
 253 (Zhao et al., 2016) between the standardised input and the reconstructed output:

$$254 \quad L_r = \frac{1}{N} \sum_{i=1}^N \left\| x_i - D_{\theta}(E_{\theta}(x_i^c)) \right\| \quad (1)$$

255 where  $x_i$  is the input standardised image,  $x_i^c$  is the corrupted standardised image,  $\|\cdot\|$  is the l1-loss,  $N$  is the batch size,  $D_{\theta}$  and  $E_{\theta}$   
 256 are namely the decoder and encoder parts of the model with  $\theta$  designating their learnable parameters.

257 The second learning task included in the training process is based on contrastive learning. Since the presented self-supervised  
 258 process does not rely on labels for the training data contrary to the vision transformer from Dosovitskiy et al. (2020), the learning  
 259 task needs to be adapted. To this extent, several geometric transformations and perturbations are applied to the training samples  
 260 for which the transformer should produce similar outputs. The synthetic pairs can then be used as matching pairs and a metric  
 261 can be built measuring their similarity. The contrastive task is thus training the model to minimise the distance between matching  
 262 pairs of sample and corresponding augmented sample, while maximising the distance between different samples in the batch.  
 263 Atito et al. (2023) propose to use as a contrastive metric the arithmetic mean over the matching pairs in the batch of the cross  
 264 entropy of their normalised similarities:

$$265 \quad L_c = -\frac{1}{N} \sum_{i=1}^N \log l_c(x_i, x_i^a, E_{\theta}, D_{\theta}) \quad (2)$$

266 where the similarity metric between a sample  $x_i$  and its augmented version  $x_i^a$  is the normalised temperature-scaled softmax  
267 similarity (Chen et al., 2020). The actual process of the contrastive learning further requires the use of a momentum encoder to  
268 generate different versions for the pairs of samples and their corresponding augmented samples.

269 The integral self-supervised training process consists in a combination of the two previously presented learning tasks. For each  
270 batch of samples, we create augmented versions of the samples which together constitute matching pairs. GMMML corruptions are  
271 applied to both samples and the model is subsequently trained to reconstruct the original inputs from these corrupted samples. At  
272 the same time, the similarity between matching pairs of samples is maximised. The complete loss function thus takes the form of:

$$273 \quad L = \alpha \times L_r + L_c \quad (3)$$

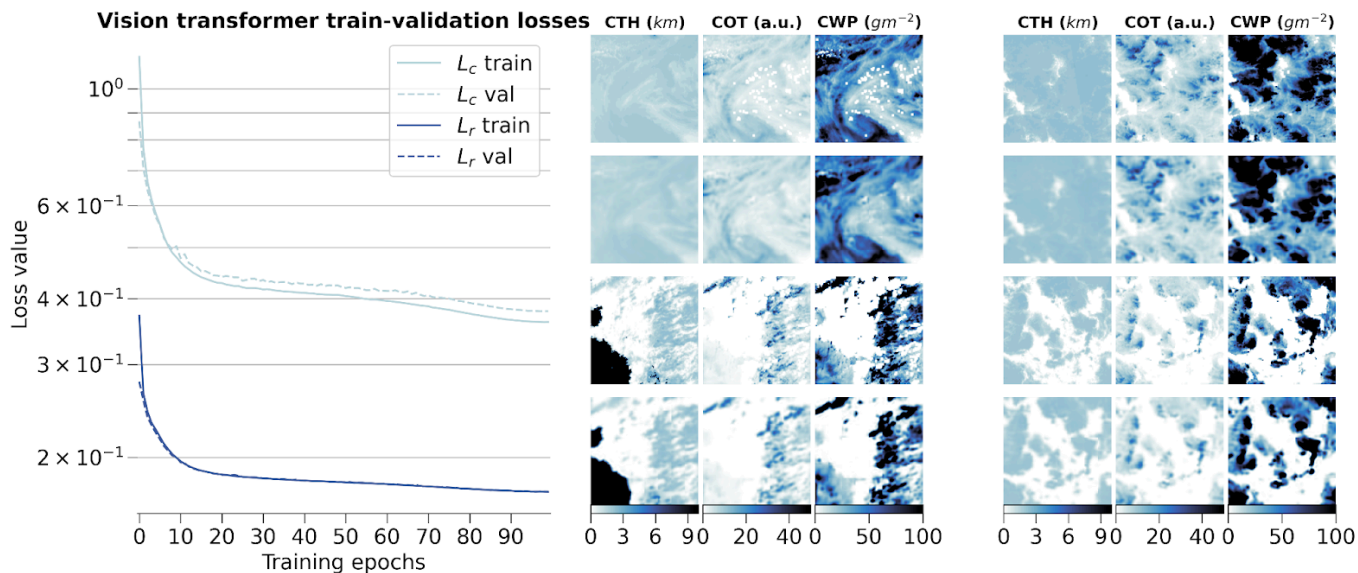
274 where  $\alpha$  is a scaling factor between the two tasks. We follow the recommendation of Atito et al. (2023) to set  $\alpha = 5$  in the case  
275 of small-scale datasets so that the vision transformer can learn enough of the local inductive bias.

276 We set out to examine in further detail the ability of the vision transformer and of the self-supervised training methodology by  
277 evaluating how different configurations of the input data and of the model architecture can impact the quality of the learnt  
278 representations and the transfer to cloud classification. We mainly discuss in this section the reconstruction skill of the vision  
279 transformer and the potential influence of contrastive learning. The transfer to the cloud classification task will be described in  
280 the following section where fine-tuning to the downstream task or the use of external models are surveyed. Since training vision  
281 transformers requires large computing resources, we limit ourselves for all the pretraining processes to only 10% of the initial  
282 dataset mentioned in section 2.2, similar to what is done in Atito et al. (2023) regarding ablation studies.

283 To begin with, we investigate how the two architectures of vision transformers fare during the self-supervised training and how  
284 the scaling factor between the contrastive loss and the reconstruction loss impacts the learning process. The two architectures  
285 tested correspond to the small variant of the vision transformer from Atito et al. (2023) and the base variant from Dosovitskiy et  
286 al. (2020). To offer an overview on each model’s complexity, their respective numbers of parameters are 21M and 86M, the main  
287 difference originating from the number of heads in the self-attention layers, the size of the multi-layer perceptron (MLP) and the  
288 hidden dimension. We additionally investigate the self-supervised training process by using pre-trained weights made available  
289 in Atito et al. (2023) for which the pretraining was done on a computer vision task, the ImageNet-1K dataset (Deng et al., 2009).  
290 However, the pretrained weights of the ImageNet-1K dataset are only made available for the small variant of the vision  
291 transformer. An additional comparison is done with a model trained only on the colocated dataset using the small variant. The  
292 contrastive and reconstruction losses for the different model setups are detailed in Figure B.1. Firstly, we notice that the model  
293 trained solely on the colocated dataset would need more epochs to reach similar performance compared to all the other setups. As  
294 the colocated dataset contains two orders of magnitude less samples than the training dataset, the model has also seen much less  
295 data after 10 epochs, hindering the training process most notably for the contrastive loss. Even after further training the model on  
296 the colocated dataset for 150 epochs, it is struggling to match the other models trained on the complete training dataset with best  
297 contrastive and reconstruction losses of 0.95 and 0.23, respectively. On the other hand, the other setups reach similar  
298 performance in both contrastive and reconstruction losses after 10 epochs. The model with pretrained weights displays better  
299 performance right from the start of the training process but improves only marginally thereafter. This could be explained by the  
300 fact that using the pretrained weights allows the model to capture already well the structure and patterns of the clouds in the  
301 remote sensing data even though their modality is different from the one seen in the ImageNet-1K dataset. It thus shows the  
302 strength of transfer learning in computer vision tasks. Nevertheless, we can observe that for the pretrained model both the  
303 contrastive and reconstruction losses are reaching a plateau after only a few epochs while the other model setups display a  
304 negative gradient indicating further learning capabilities. Focusing on the different variants trained with scaling factors of 1 or 5,  
305 we notice that the choice of a larger scaling factor leads to better reconstruction skill while losing almost no performance with  
306 respect to the contrastive loss.

307 Eventually, we decide to use as model the small variant of the vision transformer with a scaling factor  $\alpha$  of 5, as it showcases  
308 good performance in both tasks during the training while having a number of parameters four times smaller than the base variant.  
309 Furthermore, the self-supervised training task on the large unlabelled dataset allows the model to have plenty of data to learn  
310 from, the pre-trained model weights giving only marginal gain for a few epochs at the start. The small variant of the vision  
311 transformer was shown to perform very well on a large variety of tasks as per the results from Atito et al. (2023). The results  
312 across the training, validation and test datasets are shown in Figure 3 for the training process and some examples of reconstructed  
313 samples belonging to all three splits, while Figure 4 highlights the spatial distribution of the reconstruction error per channel and  
314 across splits. On the left panel of Figure 3, the losses show a consistent decreasing trend even at the end of the training epochs.  
315 The training process was halted after 100 epochs due to computational limitations, but would gain to be extended as the vision  
316 transformer’s performance seems to still be improvable. On the right panel of Figure 3, the reconstructions presented for some

317 random samples reveal where the model would benefit from an improved performance: the reconstructions appear realistic, but  
 318 fail to reproduce the exact sharpness that is visible in the satellite retrievals. While this aspect would not guarantee a decisive  
 319 improvement in the downstream task which only relies on the encodings, it would greatly help build more trust in the model. A  
 320 related case that can lead to observed patterns of reconstruction errors in Figure 4 lies in the reconstruction of cloud scenes with  
 321 convective cells. The invigorated core of the convective cell stands much higher and holds more water compared to its  
 322 surroundings which can lead to steep gradients in the cloud quantities when observed from space. As the reconstructions are not  
 323 able to reproduce these features, larger errors can arise from such cloud scenes. This could further propagate to the classification  
 324 performance on the related classes, e.g. mesoscale convection clouds or cumulonimbus, whose intricate patterns are better  
 325 assessed on their own directly (Bony et al., 2020; Rasp et al., 2020; Stevens et al., 2020; Yuan et al. 2020; McCoy et al., 2023).  
 326 The additional patterns in the reconstruction error of Figure 4, in particular for COT, are visible in some consistent areas over  
 327 land. A deeper analysis of the spatial generalisation skill of the model than the one presented in section 3.3.2 covering only the  
 328 colocated dataset might help constrain the spatial generalisation performance of the vision transformer and infer potential  
 329 performance caveats still remaining.  
 330 Ultimately, we can compare the skill of the vision transformer to that of the baseline CNN autoencoder from Lenhardt et al.  
 331 (2024a). The CNN autoencoder was trained using as reconstruction error the mean squared error (MSE) on similar MODIS data  
 332 but only with MODIS granules over the ocean. It was shown to perform similarly with a slightly higher error over land when  
 333 evaluated over a global dataset. The vision transformer model outperforms the CNN autoencoder on all metrics (MSE and  
 334 l1-loss) across all data splits (training, validation and test), displaying consistently across data splits on average an MSE of 0.15  
 335 and a l1-loss of 0.12 compared to 0.3 for both metrics for the CNN. Examples of reconstructed samples additionally show how  
 336 the l1-loss helps produce sharper edges in the reconstruction, a well-known issue with the application of MSE as target metric in  
 337 computer vision (Zhao et al., 2016). The contribution to the error comes mostly from the COT channel for both models and the  
 338 error is concentrated in areas of higher variability for the respective channels. The metrics values are summarised in Table B.1.  
 339 The spatial generalisation skill, alongside the sensitivity to the tile size and the impact of data augmentation on the performance  
 340 on the cloud classification task are analysed in the following section.



341  
 342 **Figure 3: (left) Training and validation losses during model optimization for the small variant of the vision transformer**  
 343 **on the global training dataset. (right) Examples of tiles (first and third rows) with the corresponding reconstructions**  
 344 **(second and fourth rows) for the different cloud property channels.**

### 346 3.3 Cloud type classification

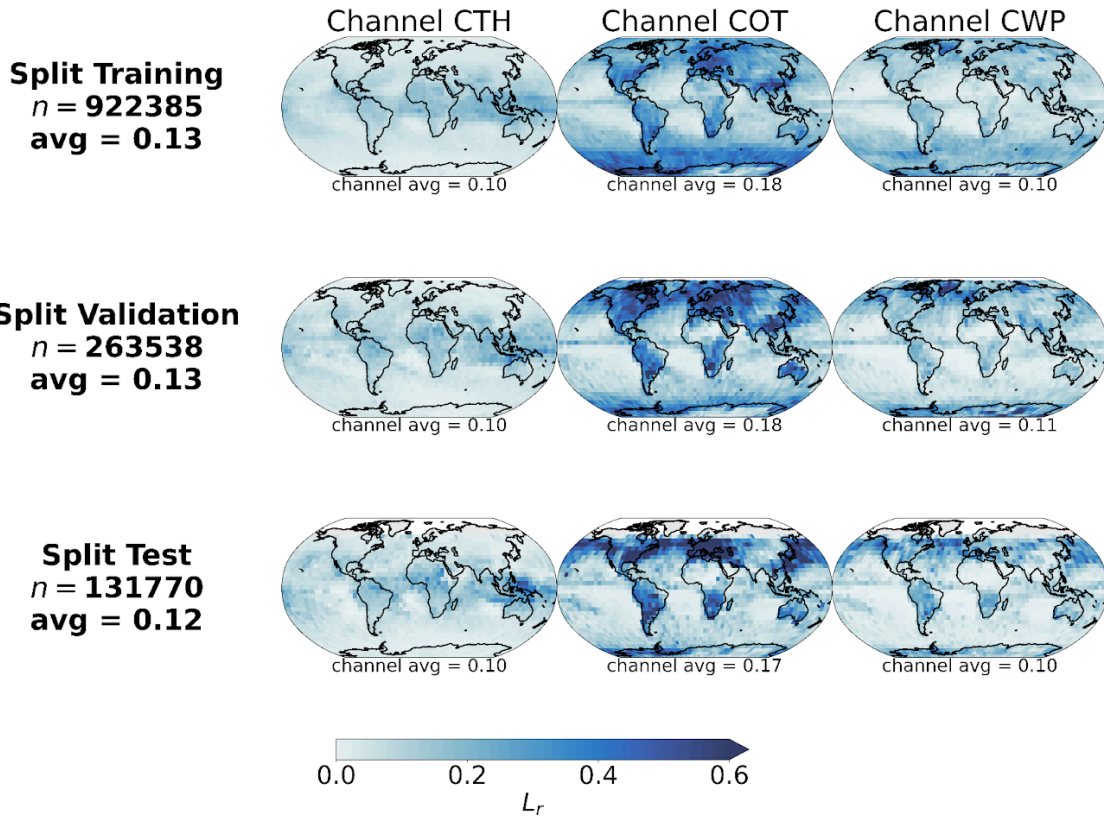
347  
 348 The next task at hand is the cloud type classification, building on the colocated samples of satellite retrievals and surface  
 349 observations. For the two years of MODIS AQUA data available, out of 104 823 colocated samples we retain only 11 094 for our  
 350 training and testing datasets after filtering, among others, for missing data - typically 50% of the samples are discarded, mainly  
 351 when the colocated observation lies on the edges of the satellite granule - and single layer cloud observations as reported by the  
 352 observer - around 60% of the previously filtered samples are kept. A main caveat arising from colocating these two data sources  
 353 is the potential mismatch between the actual clouds jointly depicted. Contrarily to methods like Zantedeschi et al. (2019) which

354 relies on joint retrievals of cloud properties and cloud type or Kuma et al. (2023) which aggregates observations at daily time  
355 scales, the presented colocated dataset leaves room for misaligned surface observations and satellite retrievals. As it will be also  
356 highlighted later on, this potential misalignment between data sources constitutes a hurdle in the development of the cloud  
357 classification method. Indeed, if the model needs to learn from satellite data that actually does not visibly fit the surface  
358 observation, then the learning process is hindered. Attempts to reduce this risk have not yielded satisfying results. For example,  
359 decreasing the time-window described in section 2.2 did not ultimately yield improvements in the classification performance,  
360 especially due to generalisation limitations from a lower number of samples. Furthermore, these attempts are mainly limited by  
361 the amount of satellite data that would be necessary to build a substantial and consistent colocated dataset which would span a  
362 larger timeframe than the two years used in this study. After the filtering of the colocated dataset, the cloud type observations are  
363 then regrouped into 4 or 10 types as mentioned previously. The rest of the study will focus on these categories as targets. From  
364 the latent space representations produced by the vision transformer or the CNN autoencoder, we build a classification model  
365 either by attaching a classification head to the encoder network or by using a simpler classification model like a random forest  
366 (RF; Breiman, 2001). To investigate the performance of the classification models on the two classification tasks at hand (4 and  
367 10 cloud types), we use different metrics tailored to unbalanced classification setups as the cloud types are not equally  
368 represented (see Figure 2 and Table A.1). A first method to assign similar weight to all classes regardless of the class' cardinality  
369 is to use macro-averaged metrics. In this framework, the metric of interest is averaged over the samples of each class separately  
370 before being averaged over the classes. This leads to a higher weight for minority classes for which the model might perform  
371 differently, usually worse, compared to the majority classes providing different information over traditional averaging strategies  
372 (micro-averaged for example) where the result will be dominated by the samples from the majority classes. We report several  
373 metrics adapted to an unbalanced setting: the index balanced accuracy (IBA; Garcia et al., 2012) of the geometric mean, the  
374 macro-averaged accuracy and the macro-averaged f1-score.

375 For the classification model we investigate two alternatives: a RF classification model (implementation from *Scikit-learn*  
376 package, Pedregosa et al., 2011) and a MLP classification head (Hinton, 1989; implemented in *PyTorch*, Paszke et al., 2019).  
377 However, a wider diversity of classification models could be implemented based on the backbone provided by the vision  
378 transformer. The base model architecture and weights are made available on Zenodo (Lenhardt et al., 2024b) to foster a more  
379 complete exploration of possibilities regarding the classification model, building on the backbone of the vision transformer. For  
380 example, with a more extensive training dataset, more complex classification models could be explored. In the case of the  
381 architecture presented here, the RF model provides simplicity in the implementation and the training process, while the MLP is  
382 the typical architecture used for the downstream task following a network like a vision transformer or a CNN. The RF model has  
383 10 or 25 trees, for the cases of 4 and 10 cloud types respectively, with a maximum depth of 5. Basic hyper-parameter  
384 optimization showed that with the reduced amount of samples and the limited variety in cloud scenes for some categories (even  
385 more with balanced classes, see section 3.3.3), models displaying limited complexity avoided overfitting and generalised better  
386 on unseen data. The MLP consists of two fully-connected layers (hidden dimension 4096) with a Gaussian Error Linear Unit  
387 (Hendrycks & Gimpel, 2016) in between and is trained using the cross-entropy loss. The sensitivity studies and experiments are  
388 done only using RF models but the evaluation in the subsequent section will be done on both types of classification methods.  
389 Various sensitivities could be explored in the presented setting but we here focus on the potential benefit of the spatial context,  
390 the ability to generalise spatially to unseen locations and the impact of balancing the labelled dataset.

391

## Spatial $L_r$ mean per channel



392

393

**Figure 4: Spatial distributions of mean channel reconstruction errors for CTH, COT and CWP, aggregated on a 5° regular grid for the training, validation and test datasets.**

394

395

### 396 3.3.1 Spatial context and tile size

397 We look at the influence of the input size by training vision transformers (small variant) on different sizes of inputs namely  
398 128x128, 64x64, 32x32 and 16x16. We do not consider larger tile sizes as the cloud scene might then be less representative of the  
399 surface observation, especially since we only consider samples with single labels, and as the assumption that the observed cloud  
400 type occurs on such scales would likely not hold. The losses relative to the vision transformer models trained on the different  
401 input tile sizes are detailed in Figure B.2. Since these models were trained on a reduced dataset as mentioned previously, their  
402 skill cannot be directly compared to the one displayed in Figure 3. While the contrastive losses are similar across input tile sizes,  
403 the reconstruction losses differ. Since we kept the ratio between the patch size and the tile size constant when training the  
404 different models, the difference in reconstruction skill could be attributed to the dimensionality of each patch being much  
405 smaller, for example for a tile of size 16x16 a patch will be 2x2. The reconstruction head being a fairly shallow CNN, the  
406 reconstruction of the spatial patterns inside the patches showcases better skill for smaller input patches after a few epochs, while  
407 for larger patch sizes - and thus tile sizes - a longer training process would be needed as to improve the truthfulness of the  
408 reconstruction to the input. Examples of reconstructions depending on the input tile size are included in Figure B.3 and visually  
409 display how a larger field of view can help capture the larger cloud organisation or even individual sparse clouds. To further  
410 evaluate the potential benefit of the spatial context for the downstream classification task, we consider as an alternate input the  
411 flattened cloud properties of a 9x9 tile centred on the observation location. This yields an input of similar dimensionality  
412 compared to the latent space representation of both the CNN and the vision transformer (3 channels x 9 x 9 = 243). We then train  
413 the same RF classification model on each of the latent representations derived from the trained vision transformers and on the  
414 flattened cloud properties. From the classification metrics, we observe that the smaller the tile size the more prone the model is to  
415 overfitting towards the majority classes (high and stratiform cloud types in the case of 4 types) leading to a decreased  
416 performance on the validation set. For instance, choosing an input tile size of 16x16 results in a decrease of 20% across metrics  
417 from the training to the validation set (compared to around 10-15% across metrics for the larger input tile sizes), and leads to  
418 metrics on the validation set more than 10% lower than with larger input tile sizes. The predictions made using larger spatial  
419 context (tile size greater than 16x16) outperform the method with 9x9 flattened tile inputs across all considered metrics on the

420 validation set. With the input tile size 16x16, the reduced spatial context seems to be limiting for the performance but another  
421 explanation could be a complex latent space compared to the input dimensionality. Overall, even with the vision transformer  
422 backbones being trained only partially, the wider input tile size provides better classification skill and generalisation to unseen  
423 data. In the rest of the study and experiments, if not mentioned specifically, the input tile size is chosen to be 128x128.

424

### 425 3.3.2 Spatial generalisation

426 To investigate the spatial generalisation skill of the cloud classification method, we split our colocated dataset into samples  
427 located in the Northern or Southern hemispheres. Two vision transformer models are additionally trained on samples from only  
428 the respective hemisphere and tested on the other one. The losses relative to the training and testing of both hemispherical  
429 models are included in Figure B.4. Both hemispherical models display similar performance both on the training and testing  
430 datasets, showing that even for a reduced number of training samples, epochs and spatial coverage the vision transformer  
431 architecture generalises well to unseen data. Building on the two trained vision transformers, we set out to evaluate the skill on  
432 the classification tasks. Splitting the labels between the two hemispheres yields 9246 samples for the Northern hemisphere and  
433 1848 samples for the Southern hemisphere. Investigating the different classification metrics for training and testing on both  
434 hemispheres, it is clear that the classification model trained on the Southern hemisphere struggles to generalise from such a low  
435 number of labelled samples and probably overfits since the performance is worsened on the Northern hemisphere samples  
436 (decrease of almost 50% across metrics from the training to the testing set). The classification model trained on the Northern  
437 hemisphere generalises well in the case of the 4 cloud types with consistent metric values between hemispheres (marginal  
438 decrease of around 15% across metrics from the training to the testing set). Overall, the model trained on samples from the  
439 Northern hemisphere and for both cases of number of cloud types, the performance on the Southern hemisphere is similar to  
440 models with larger tile sizes from the previous section, showing consistency across experiments even with limited datasets for  
441 the training of the vision transformer.

442

### 443 3.3.3 Balanced training dataset

444 Balancing the number of samples among classes in the input dataset can be a way to leverage enough information from the  
445 underrepresented classes. We compare here the performance skill of two classification models trained on the colocated dataset or  
446 on a balanced equivalent. To this extent, we use a sampler implementation from the *imbalanced-learn* package (Lemaitre et al.,  
447 2017), namely the Synthetic Minority Oversampling Technique (SMOTE; Chawla et al., 2002) to oversample the minority  
448 classes. Doing so leads to improved classification skill with consistent increases across metrics on the validation set of 3-7% and  
449 15-35% for the cases of 4 or 10 cloud types, respectively. The oversampling impacts mostly the cloud types from the high and  
450 medium classes, and from the cirrocumulus and cirrostratus classes, in the case of 4 cloud types and 10 cloud types, respectively  
451 (see Table A.1). The methods evaluated in the following section will thus include the same over-sampling strategy to overcome  
452 the representation of the minority classes and improve the performance on the classification task.

## 453 4 Evaluation

454

### 455 4.1 Classification evaluation

456

457 In the following section, we detail the classification performance on the test set of the previously mentioned models. Two  
458 baseline models are included, namely a classification model built on the CNN autoencoder from Lenhardt et al. (2024a) and a RF  
459 model built on the flattened 9x9 input tiles as described in section 3.3.1. The method developed in this study is represented by  
460 two models using the aforementioned vision transformer model (see section 3.2) as backbone complemented by either a RF  
461 classifier or a MLP (see section 3.3). In the rest of the study, we denote the trained vision transformer model followed by the  
462 classification model as CloudViT (Cloud Vision Transformer) in its two classification variants (RF or MLP). The classification  
463 metrics on the test dataset for these four models are summarised in Table 2 for the case of the 4 cloud types and in Table C.1 for  
464 the 10 cloud types. Since the number of samples is very limited, the performance of the models cannot be only considered as is  
465 but is further evaluated in the subsequent sections through distributions of cloud properties and spatial occurrence distributions.  
466 We emphasize here the need to perform an evaluation beyond the metrics to assess the skill of the model to represent  
467 characteristics expected from different cloud types. These characteristics can relate to the distribution of their physical  
468 parameters and their occurrences, both of which can be assessed thoroughly here only with a more extensive dataset. The  
469 CloudViT/RF method performs the best across all of the three metrics included, despite showing still limited performance overall.  
470 Firstly, the macro-averaged multi-class accuracy does not differ by a large margin between the different methods, but the

471 class-wise accuracies reveal several limitations. The baseline 9x9 RF model largely overfits towards the high and stratiform types  
472 (train and test class accuracies of 0.84/0.81 and 0.63/0.62, respectively), performing poorly on the medium and cumuliform types  
473 (train and test class accuracies of 0.31/0.21 and 0.19/0.15, respectively). The CloudViT/MLP model is biased towards stratiform  
474 clouds (train and test class accuracy of 0.79/0.79) while struggling to identify the other three types (train and test accuracies all  
475 falling between 0.10 and 0.40). The baseline CNN/RF and the CloudViT/RF models are performing quite similarly both on  
476 aggregated and class-wise metrics. However, the CloudViT/RF model showcases improved performance on the stratiform class  
477 (increase of 0.13 in the class accuracy both on the train and test datasets) and only a marginal decrease (0.03) on the class  
478 accuracies for medium and cumuliform clouds. The performance on the high clouds is similar with slightly higher accuracies for  
479 the CloudViT/RF model. Other metrics like the IBA of the geometric mean and the F1-score further emphasise that the  
480 CloudViT/RF model outperforms the other methods while addressing the imbalance training data to generalise with satisfactory  
481 skill on the unseen test dataset. Nevertheless, the performance detailed here across classes shows apparent limitations as scores  
482 are not ideal. An obvious hurdle of the learning process resides in the overall limited number of samples and the noise present in  
483 particular for cloud types with minimal numbers of samples. Building a dataset with more labels would improve the  
484 classification performance by allowing the classification to more easily converge towards each cloud type’s mean state arising  
485 from a larger number of samples. The simplicity of the classification models chosen here represents a constraint that could be  
486 lifted if more training samples were available as overfitting and balance would then represent lesser issues. Furthermore, the  
487 patterns in the class accuracies can be traced back to shortcomings in the observational dataset. Having only considered  
488 single-layer cloud scenes in the colocated dataset, the high clouds are well predicted in accordance with the observations as a  
489 surface observer would identify with certainty this type of cloud if no other lower cloud is blocking the field of view from the  
490 surface. Stratiform clouds could be more challenging for the observers as they typically display high cloud fraction and high  
491 optical thickness, limiting the ability of the surface observer to quantify with certainty the amount of clouds in other levels.  
492 However, such characteristics can be well captured by computer vision models which build on patterns in the three-dimensional  
493 input data which in particular the baseline 9x9 RF model lacks. This difference between models is in particular apparent for the  
494 cumuliform class which is mostly composed of observations of cumulus. A cloud scene relative to a cumulus observation will  
495 most likely display a lower cloud fraction as the individual clouds are sparsely distributed, extracting only the very near points  
496 around the observation might then be too reductive and limit the accuracy of the classification model. It is confirmed by the  
497 accuracy on this cloud type for which the baseline 9x9 RF model is largely outperformed by all three other models both on  
498 training and test datasets (class accuracy increases between 150% up to 260% on the test dataset). Overall, the classification  
499 model shows fair performance that could be probably improved by widening the scope of the cumbersome collocation process  
500 which requires large amounts of remote sensing data, and by accordingly refining the RF or MLP architectures presented here.  
501 Using the classification model developed here thus comes with apparent uncertainties across the different cloud types. Efforts  
502 were made with the aim to classify all cloud types consistently from the limited training dataset available but to limited  
503 outcomes. The extension of the training dataset appears as an obvious way to purposefully improve the classification  
504 performance of the model. An extended colocated dataset would allow stricter filtering, mainly with respect to the collocation  
505 time-window, which would help improve the representativeness of the samples. The analysis of the classification performance  
506 shows here the limitations of a reduced-size dataset with potential underlying discrepancies between data sources during  
507 collocation. Nonetheless, the evaluation of the predictions in the following section provides insights and reveals relevant features  
508 in the predicted cloud types.

509

Method	Multi-class accuracy *	IBA geometric mean	F1-score *
Baseline 9x9 RF	0.45	0.32	0.35
Baseline CNN/RF	0.45	0.32	0.40
CloudViT/MLP	0.40	0.32	0.42
<b>CloudViT/RF</b>	<b>0.46</b>	<b>0.36</b>	<b>0.43</b>
CloudViT/RF (train)	0.55	0.41	0.49

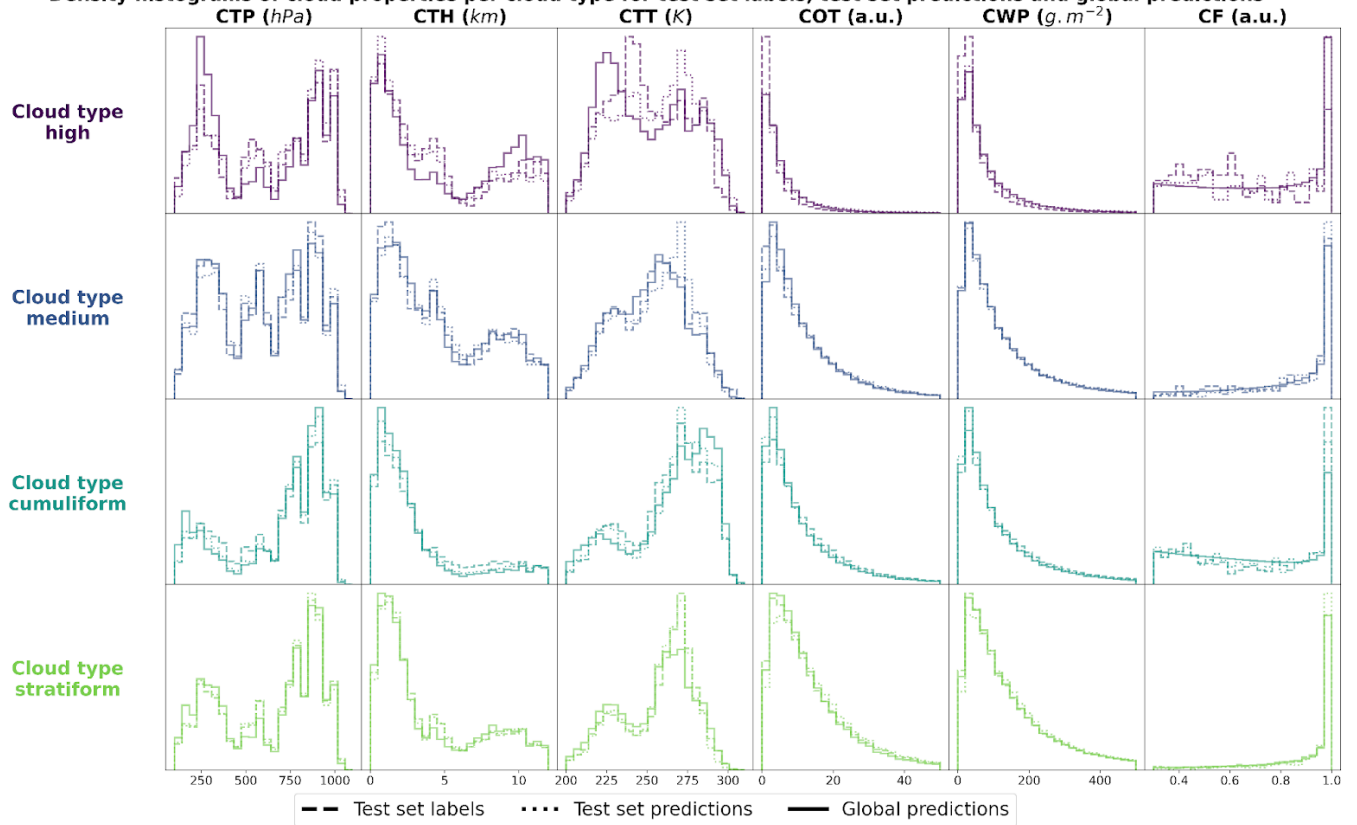
510 **Table 2: Classification metrics on the test set in the case of 4 cloud types. The metrics noted with a \* are referring to their**  
511 **macro-averaged estimate. The method on which the rest of the study is based is highlighted in bold. The baseline**  
512 **CNN/RF refers to the CNN backbone introduced in Lenhardt et al. (2024a).**

## 514 4.2 Histograms of cloud properties

515  
516 In order to evaluate the physical soundness of the predictions made by the CloudViT model, we investigate the distribution of  
517 several cloud properties with respect to the observed and predicted cloud types. In Figure 5, we summarise the distribution of  
518 cloud top pressure (CTP), cloud top height (CTH), cloud top temperature (CTT), cloud optical thickness (COT), cloud water path  
519 (CWP) and cloud fraction (CF) for the 4 cloud types (high, medium, cumuliform, stratiform) and for three different datasets: the  
520 test set labels, the test set predictions and the dataset of global predictions. The latter is built on global MODIS AQUA granules  
521 for the year 2016 - the year is chosen to avoid any overlap with cloud scenes seen during the training of the vision transformer on  
522 data from 2008 - from which we regularly sample tiles in order to build a more comprehensive and global dataset of cloud types  
523 to further evaluate the method. The spatial distribution of cloud types for this dataset is highlighted in the following section and  
524 the global dataset is made available at Lenhardt et al. (2024b). The histograms are built by reporting the respective cloud  
525 properties for all the cloudy pixels in each sampled tile from the dataset apart from the cloud fraction which is computed for the  
526 whole tile from the cloud mask. As a consequence, unless the whole cloud field is composed of only a single cloud type, the  
527 histograms will cover a large range of cloud properties due to multi-layer clouds or multi cloud types scenes (e.g. convective  
528 cells with associated anvils or cumulus/stratocumulus transitions). Even though the trained model only produces fair evaluation  
529 metrics on the test set, the histograms of cloud properties display interesting features consistent with expected characteristics of  
530 the different cloud types. On Figure 5, the histograms pertaining to the test set labels and predictions have distributions close to  
531 identical across cloud types showing a good agreement in the clouds depicted in both datasets while the global dataset histograms  
532 provides a less noisy overview of the distribution of the cloud properties per cloud type. The high clouds are characterised by  
533 low cloud water path and optical thickness, along with colder and higher cloud tops as well as more frequent cloud fractions  
534 smaller than one. All of these aspects are emphasised in the global predictions compared to the limited test set samples, showing  
535 the CloudViT model manages to extract the representative characteristics of the cloud type from the labels. The cumuliform  
536 category encompasses mostly low warm clouds with reduced cloud fractions and moderate cloud water path and optical  
537 thickness. Inside this class, the higher and colder cloud tops are concentrated in the cumulonimbus class, along with larger cloud  
538 water path and cloud optical thickness (see Fig. C.1). The stratiform class includes thick cloud fields with high cloud water path  
539 and almost full spatial coverage of the cloud scenes (cloud fraction close to 1 in most cases). A fraction of the clouds in this class  
540 are slightly higher and colder and correspond to stratus/nimbostratus clouds which can also be seen in Figure C.1. The  
541 distributions for medium clouds showcase similarities with several other types and are best evaluated in combination with their  
542 spatial distribution (see Section 5). Examining in more detail the refined cloud types with the 10 cloud types (see Fig. C.1)  
543 reveals slight differences inside broader cloud types. For example, the distinction between the three high cloud types (cirrus,  
544 cirrostratus and cirrocumulus) appears through separations in cloud fraction, cloud optical thickness and cloud water path which  
545 were not obvious from the limited amount of labelled samples. The differences between the three high cloud types further  
546 manifest in distributions of cloud top quantities for which cirrus and cirrostratus display potential multilayered cloud scenes with  
547 a combination of low/warm and high/cold cloud tops. Overall, the CloudViT model seems to generalise well from a few samples  
548 (only around 10 for the cirrocumulus class) by exhibiting in parts physical consistency inside predicted types. Due to the large  
549 cloud scenes considered as input for the classification, the distribution of the cloud properties might not be as representative of  
550 single cloud types as an input tile of, for example, 16 pixels. The main caveat regarding performance on high and medium clouds  
551 from our method is that the ground-based observer identifies these cloud types with higher uncertainty compared to that of low  
552 clouds. Additionally, stratiform clouds with high cloud fraction can hinder the trustworthiness of the surface observation if the  
553 whole field of view is cloudy. Even though the limitations of ground-based observations are evident, they still provide quality  
554 observations on which a classification model can be trained. The collocation between these surface observations and the satellite  
555 retrievals is thus of crucial importance and guides the performance of the later trained model. It partly contributes in the case of  
556 CloudViT to a hurdle to achieve notable classification performance. The model, however, shows its ability to generalise from  
557 limited samples to consistent and physically-relevant distributions of cloud properties among the predicted cloud types. By  
558 refining the training dataset, the improvements can be expected to reflect directly on the classification performance. The  
559 characteristics observed in the histograms across cloud types contribute to an increase in confidence in the ability of CloudViT to  
560 discern various cloud types in large remote sensing datasets despite the method's limited ability described in the previous section.

561

Density histograms of cloud properties per cloud type for test set labels, test set predictions and global predictions



562

563 **Figure 5: Density histograms of cloud properties for each cloud type from high, medium, cumuliform and stratiform.**

564 **5 Global cloud type distributions in MODIS data**

565

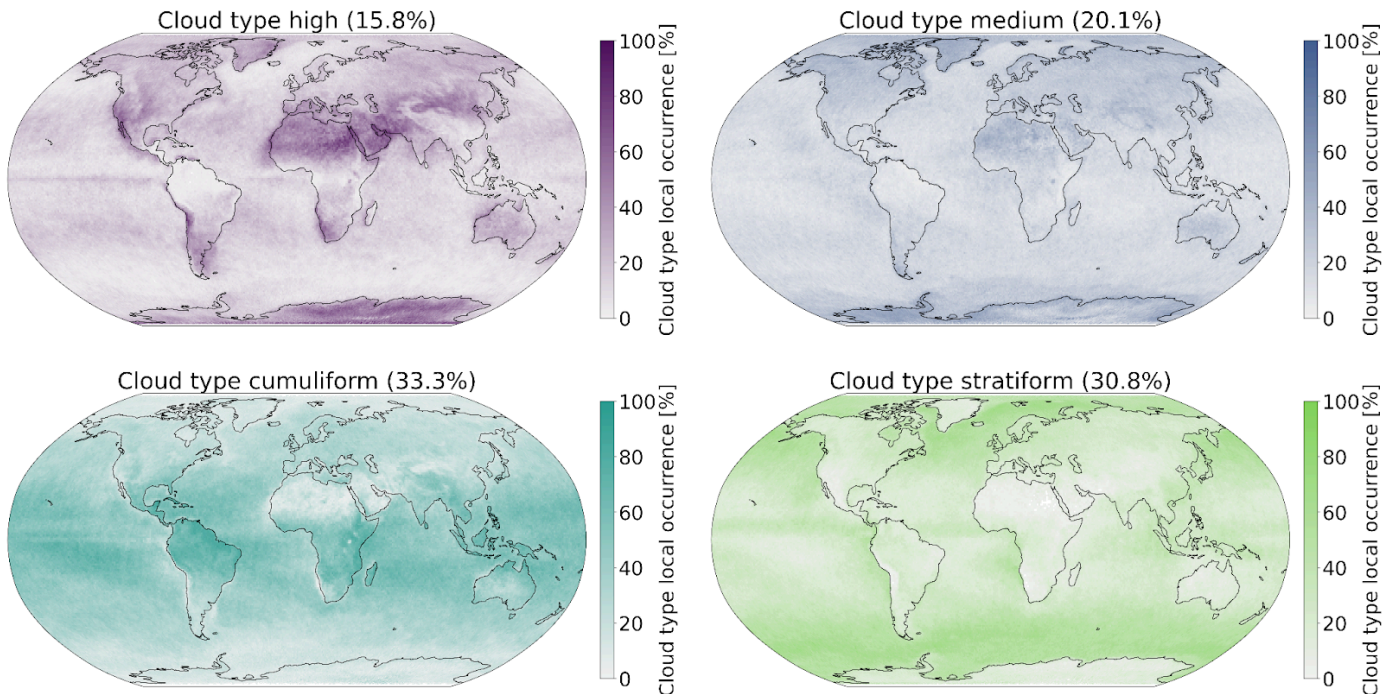
566

567 Additionally to the physical and microphysical characteristics of the different cloud types, their global spatial distribution can  
 568 help us further understand in which regions they are more or less frequent and qualitatively assess the presented classification  
 569 method compared to other remote sensing products. To this extent, as mentioned in the previous evaluation section (see Section  
 570 4), we build an extensive cloud type dataset for the year 2016 from MODIS AQUA granules which are regularly sampled for  
 571 tiles of 128x128 pixels. The sampling step (64) is chosen for computational efficiency and memory purposes to be not too small  
 572 to avoid large overlap between neighbouring tiles but large enough to ensure representativeness in the later aggregated  
 573 predictions of the MODIS granules. Furthermore, as the area covered by each tile is rather wide, the spatial distribution of cloud  
 574 types might be less smooth than other products (e.g. Sassen et al., 2008) or other methods (Zantedeschi et al., 2020) which are  
 575 providing cloud types for smaller cloud fields. Additionally, the dataset is built on single daily overpasses of the MODIS  
 576 instrument and can thus be biased towards the local retrieval time (13:30 h, early afternoon for AQUA).

577 The spatial distributions of the predicted cloud types for the global dataset for the year 2016 are detailed in Figure 6 and Figure  
 578 C.2 for 4 and 10 cloud types, respectively. Firstly, we note that CloudViT predictions capture large scale patterns which are in  
 579 agreement with observational datasets (Sassen et al., 2008; Cesana et al., 2019; Wood, 2012; Pincus et al., 2023). Stratiform  
 580 clouds, and in particular stratocumulus (see Fig C.2), are frequent in the high latitudes and along the western coasts of America  
 581 and Africa. Cumuliform clouds are concentrated in the Tropics apart from the areas where stratocumulus clouds are dominant.  
 582 Medium clouds are concentrated in the polar regions and over land in the higher latitudes. High clouds make up a large portion  
 583 of clouds in the polar regions but also over land. The first notable difference is the low occurrence of high clouds in the Tropics  
 584 which would be expected to be higher (Sassen et al., 2008; Pincus et al., 2023). An explanation could be the frequent occurrence  
 585 of high clouds in multi-layer cloud scenes related to convection in the Tropics. Furthermore, in such cases the model probably  
 586 identifies the cloud types with larger cloud fraction and thus discards potential high clouds in the scene. Incorporating more  
 587 samples of high clouds in that region (see Fig. A.1) could potentially help the performance of the classification model in that  
 588 regard. The presented spatial distributions may suffer from the somewhat limited performance of the classification model despite

589 the corresponding reasonable representation of cloud type characteristics showcased in section 4.2. Nevertheless, some  
590 informative features are observed in Figures 6 and C.2 and point towards the good direction for further improving CloudViT.  
591

### Spatial distributions of CloudViT cloud type occurrences (year 2016)



592  
593  
594  
595

**Figure 6: Spatial distributions of the CloudViT cloud type occurrences (cloud types high, medium, cumuliform, stratiform) for MYD06 granules for the year 2016 aggregated on a 1° regular grid.**

## 596 6 Challenges and limitations

597

598 The method and results highlighted in the previous sections provide useful material to further analyze the developed  
599 methodology, but also to be critical of its shortcomings. The following section aims to focus on several aspects that we feel are  
600 relevant for the community when developing cloud type classification methods similar to the one presented here, namely on the  
601 benefits of such methods, dataset curation and extension, and the potential application to climate model data.

602 Spatially-resolved cloud properties provide usable context for the CloudViT model to improve the cloud classification, as shown  
603 in the comparison to the baseline method with limited spatial information. Introducing this new transformer model architecture  
604 additionally improves the classification skill over the CNN backbone mentioned in Lenhardt et al. (2024a). Overall, CloudViT  
605 achieves passable performance even on sparsely represented classes for both cases of 4 and 10 cloud types. The limited colocated  
606 dataset proves to be a hurdle for the proper training and evaluation of the method on labelled samples but the generation of an  
607 extensive global dataset allows deeper investigation into the cloud types. Improvements could come from a more extensive  
608 training dataset which would encompass a larger variety of cloud type samples to certainly enhance the classification's  
609 performance both for the training and testing metrics. The subsequent evaluation exhibits interesting results despite the limited  
610 performance on the colocated dataset. In the global dataset, the predicted cloud types exhibit fairly physically reasonable  
611 distributions of their respective cloud properties, and their global spatial distributions are consistent in parts with other products  
612 (Section 5). Application to climate model data can prove to be technically straightforward and results in insights into how such  
613 methods can be transferred to model data (Appendix D). The necessary cloud quantities can be obtained from common  
614 simulation outputs (cloud liquid water and ice contents, altitude, droplet number) which makes methods using such inputs easily  
615 applicable to climate model simulations. Cloud type diagnostics could be a resourceful addition to the panel of assessment  
616 methods for model data (Kuma et al., 2023; Kaps et al., 2023) given improvements to achieve remarkable performance in the  
617 classification ability as previously described.

618 The hypothesis as to why the model fails to achieve great performance in this study rests heavily on the collocation process  
619 between surface observations and satellite data. The method would benefit from including further ground-based observations  
620 through the collocation process but then much larger storage and computational facilities would be needed as global MODIS data  
621 represents thousands of granules each day. More training samples could simultaneously solve performance issues by providing a  
622 clearer vision of the different cloud types for the classification model to learn from. The improvements through a larger training  
623 dataset will yield relevant benefits only if the potential mismatches occurring during the collocation process are tackled.  
624 Improving the representativeness of the training samples could solve the performance issues faced by the model presented here,  
625 and potentially achieve performance aligned with a wider usage of the method for cloud type analysis. The classification model  
626 could also be refined by finding better alternatives to the RF or MLP presented here. The overall finetuning process involving the  
627 vision transformer and the MLP classification head proved to be cumbersome but holds great promise if the labels and training  
628 process are refined. Transfer learning from a typical ImageNet-trained model did not yield a notable performance difference  
629 which shows the current need for foundation models trained on remote sensing data. The main hurdle here remains the large  
630 diversity in instruments, quantities and resolutions among remote sensing products which hinders the possibility of a unified  
631 model.

632 To improve the spatial coverage of the CloudViT predictions, the direct application to granules from MODIS TERRA would  
633 technically not require much more work as the instruments are similar and provide the same cloud properties. An additional  
634 benefit would come after the upcoming decommissioning of the CloudSat mission which was providing cloud type retrievals  
635 along its track aligned with MODIS. We would then be able to still offer information about cloud types over the same areas even  
636 though no vertical information is available and used from our predictions on MODIS level 2 data. As for other satellite cloud  
637 products, the main difference would arise, similarly to climate model data, from the potentially different distributions and ranges  
638 in the input cloud properties which would need either retraining of the vision transformer or careful scaling to match the  
639 distributions seen in MODIS data. Some limitations due to satellite retrieval shortcomings should be taken into account when  
640 applying the described method to certain areas. Indeed, since MODIS data is collected through near-nadir scanning, observations  
641 in high-latitude regions become oblique, leading to distortions and potential errors in cloud property retrievals, such as cloud top  
642 height and optical thickness.

643 Furthermore, some caveats can appear when applying such a cloud classification method to climate model data. As mentioned in  
644 more details in Appendix D, the input scaling is crucial to ensure proper portability of a method to this other data source. The  
645 absence of nighttime retrievals in the MODIS data also turns the evaluation of predictions on nighttime data points across the  
646 model data into a challenging issue. However, clouds play a role in the climate system both during the day when they cool the  
647 surface by mostly reflecting incoming solar radiation but also at night when they warm the surface by trapping outgoing  
648 terrestrial radiation. Shifts and changes in cloud occurrence and distribution in the current climate but also in future projections  
649 could further influence global climate change (Luo et al., 2024). Applying a cloud classification methodology to a limited  
650 high-resolution climate model simulation is an encouraging direction, but considering more common and computationally less  
651 expensive global km-scale simulations (horizontal resolution of 5 km for example) could be of greater interest to the community  
652 to study longer time scales. To this extent, two conceivable approaches would consist in either retraining a method like CloudViT  
653 on coarser input cloud properties matching the model data resolution - the MODIS Cloud product is also available at a 5 km  
654 resolution even though the 1 km equivalent is recommended for use - or in using such a method as is but with the coarse input  
655 scaled to fit the resolution of the tiles on which it was trained on. The first option could be more interesting as computer vision  
656 models are commonly trained on coarser resolutions first to learn the broad specificity and patterns in the data before fine-tuning  
657 the model on finer resolution (Touvron et al., 2019).

## 658 7 Conclusion

659  
660 This study introduces a new method called CloudViT to classify cloud types from MODIS cloud properties, specifically CTH,  
661 COT and CWP. CloudViT delivers estimates for either 4 (high, medium, cumuliform, stratiform) or 10 (cirrus, cirrostratus,  
662 cirrocumulus, altostratus, altocumulus, cumulus, cumulus and stratocumulus, cumulonimbus, stratocumulus, stratus) cloud types  
663 with fair performance. The classification model was built on ground-based observations of cloud types (Section 2.1) and  
664 experiments about its generalisation skill and the benefits of spatial information were presented (Section 3). We evaluated the  
665 classification model by examining distributions of cloud properties in Section 4 and the global spatial distribution of cloud types  
666 in Section 5. Lastly, we pinned down some existing challenges, limitations, and lessons learned from the development of the  
667 method for cloud type classification. The global dataset alongside the CloudViT code and weights are made available on Zenodo  
668 (Lenhardt et al., 2024b) to encourage future developments.

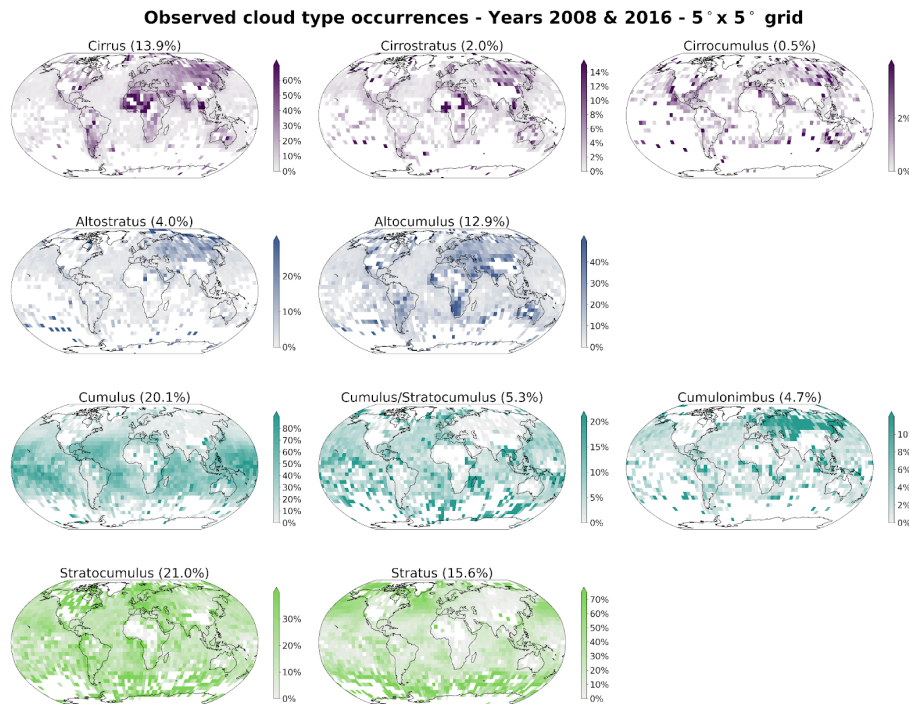
669

670 In conclusion, the method presented here showcases and highlights a wide array of potential applications in the study of cloud  
671 types, their characteristics and evolution, and their past, current, and future effects on the Earth's climate: from the extension of  
672 sparse surface observations to global yearly predictions, and existing challenges and limitations in the design of  
673 vision-transformer-based models. Despite the relatively imbalanced performance assessment of the method which shows both  
674 great promise in capturing large scale characteristics of cloud types distributions but struggles to capture precisely the features in  
675 the training dataset, the design and development of CloudViT is an interesting study in the line of improving existing cloud  
676 classification methodologies. Identified challenges and limitations in this particular case can be useful to the community, both in  
677 terms of methodology development and caveat to be avoided. We recommend future advancements in cloud classification  
678 methods like CloudViT being firstly focused on data curation and followingly on model tuning once the performance has been  
679 raised to desirable levels. To this extent, the necessary datasets and model architecture code are made available on Zenodo  
680 (Lenhardt et al., 2024b).

682 Appendix A: Cloud type observations

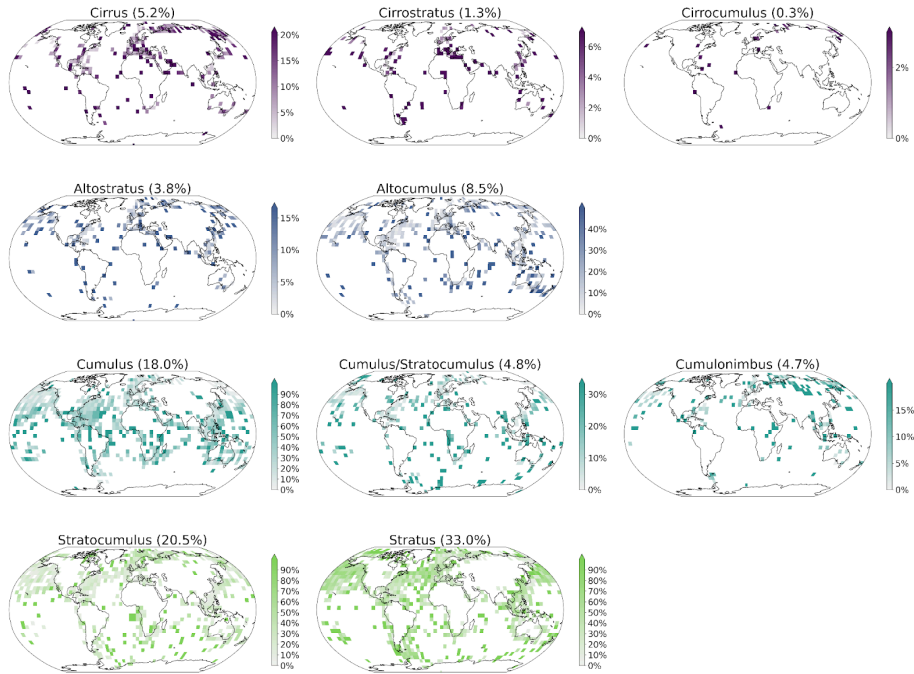
WMO codes	Cloud type: 4 groups	Cloud type: 10 groups	Colocated samples
High clouds 1-6	High	Cirrus	n = 574
High clouds 7-8		Cirrostratus	n = 142
High clouds 9		Cirrocumulus	n = 29
Medium clouds 1-2	Medium	Altostratus	n = 420
Medium clouds 3-9		Alto cumulus	n = 944
Low clouds 1-3	Cumuliform	Cumulus	n = 1998
Low clouds 8		Cumulus and stratocumulus	n = 533
Low clouds 9	Stratiform	Cumulonimbus	n = 519
Low clouds 4-5		Stratocumulus	n = 2274
Low clouds 6-7		Stratus	n = 3661
Total			n = 11 094

683 Table A.1: Cloud types from the WMO observational datasets, their groups following Kuma et al. (2023) and the  
 684 corresponding number of samples in the colocated dataset. The WMO codes correspond to the 9 types for each level.

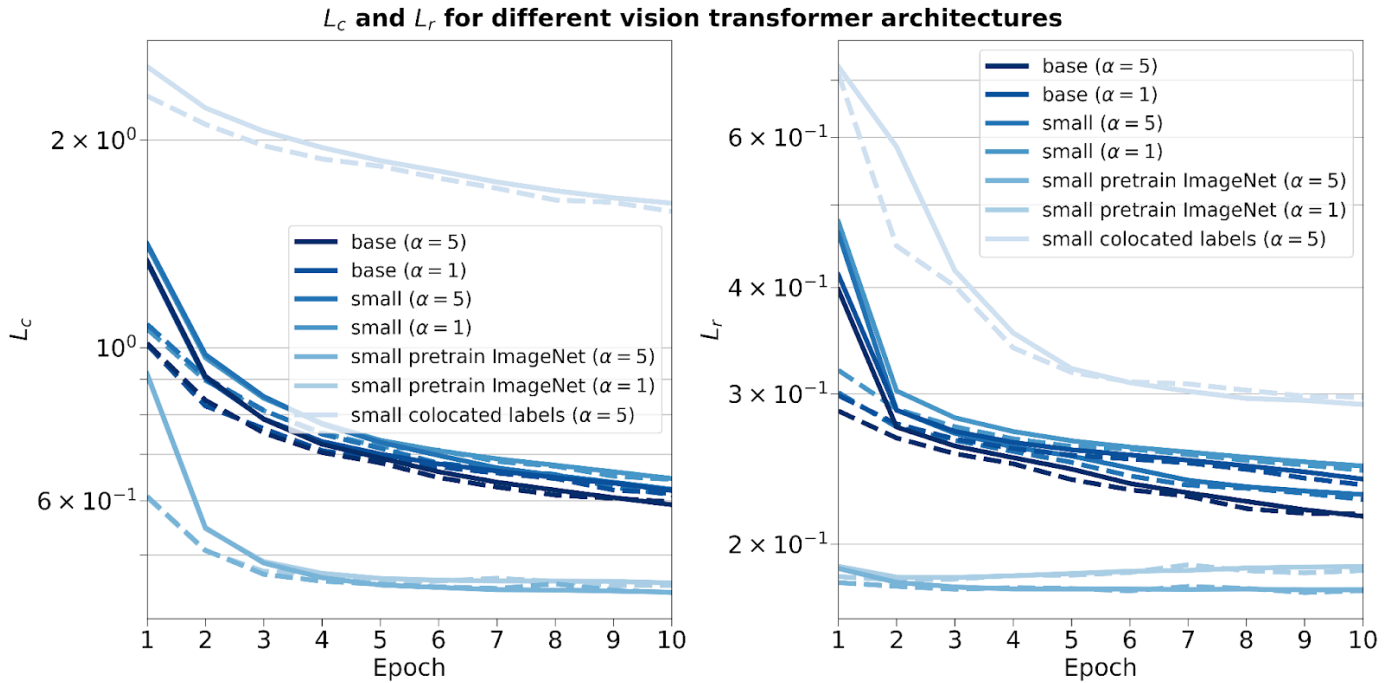


685  
 686 Figure A.1: Spatial distributions of observed cloud types (cloud types cirrus, cirrostratus, cirrocumulus, altostratus,  
 687 alto cumulus, cumulus, cumulus and stratocumulus, cumulonimbus, stratocumulus, stratus) from the Met Office datasets  
 688 (Met Office, 2006; Met Office, 2008) for the years 2008 and 2016. Overall percentage of each label in the total dataset is  
 689 indicated in brackets.  
 690

Observed cloud type occurrences - Colocated dataset - 5° x 5° grid



691  
 692 **Figure A.2: Spatial distributions of observed cloud types (cloud types cirrus, cirrostratus, cirrocumulus, altostratus,**  
 693 **altocumulus, cumulus, cumulus and stratocumulus, cumulonimbus, stratocumulus, stratus) from the Met Office datasets**  
 694 **(Met Office, 2006; Met Office, 2008) for the years 2008 and 2016 colocated with the satellite cloud retrievals (Platnick et**  
 695 **al., 2017) used for training the classification model. Overall percentage of each label in the total dataset is indicated in**  
 696 **brackets.**



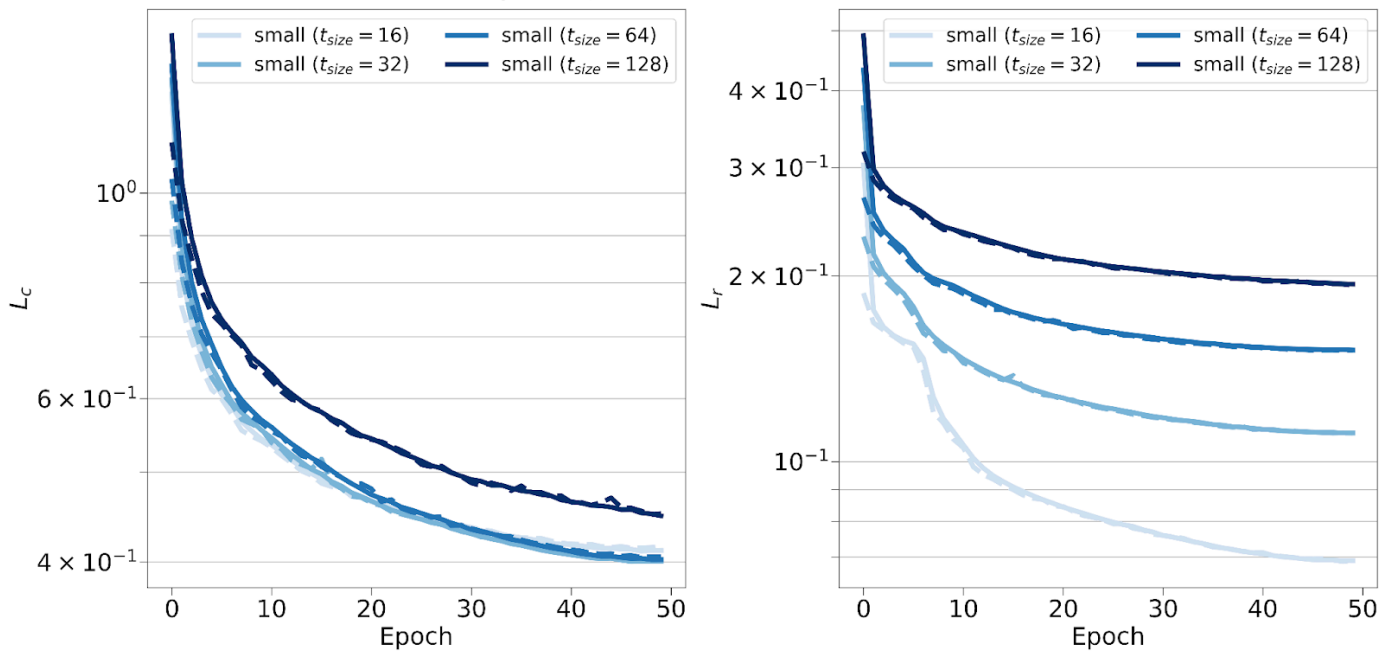
702 **Figure B.1: Training and validation contrastive (left) and reconstruction (right) losses for different vision transformer**  
 703 **architectures, pretraining weights, training datasets and scaling factor  $\alpha$ .**

705 **B.2 Reconstruction errors for the CNN autoencoder and the vision transformer (small variant) on the test set**

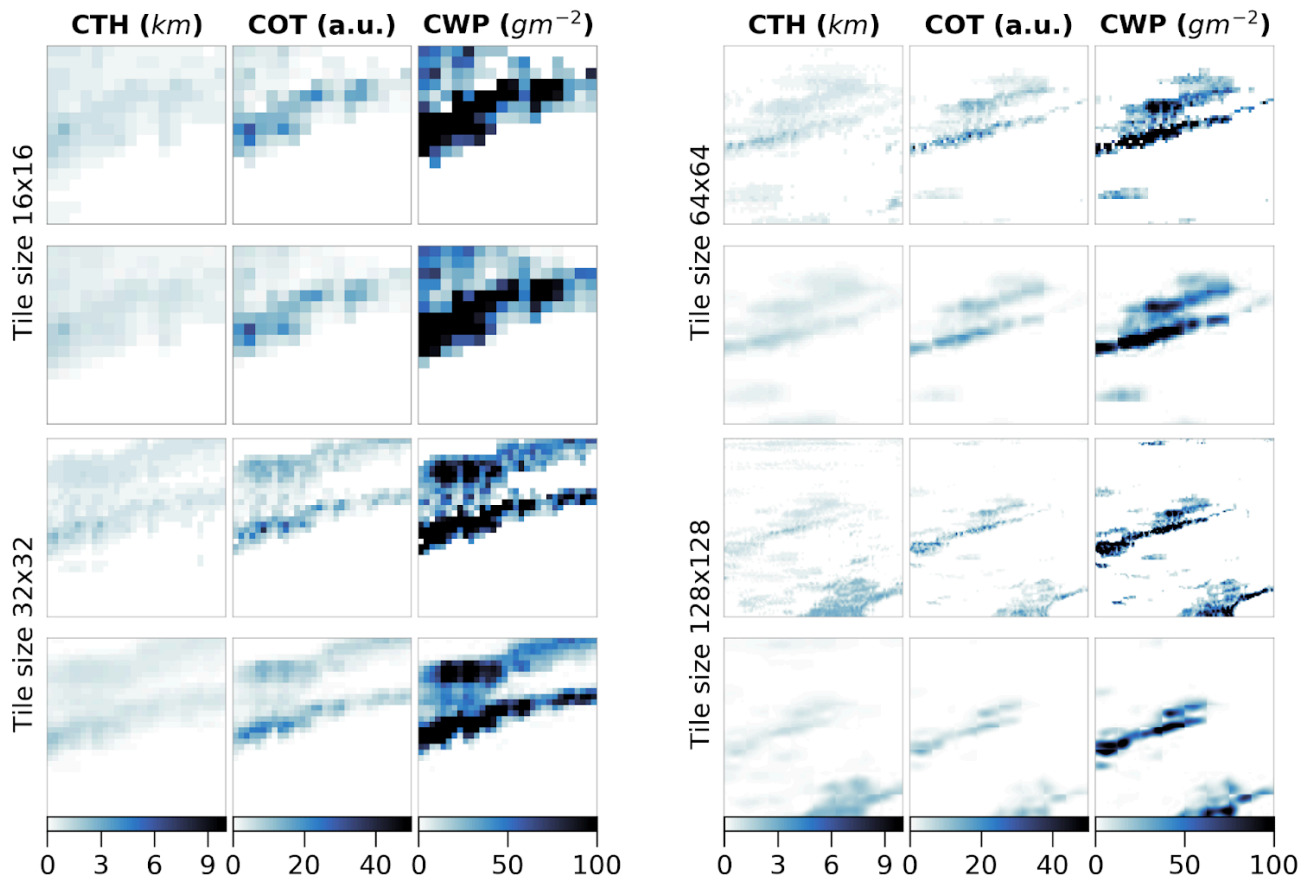
Model type	Reconstruction error	CTH	COT	CWP
CNN autoencoder	MSE	0.27	0.39	0.25
	l1-loss	0.36	0.33	0.21
Vision transformer (small variant)	MSE	0.06	0.25	0.13
	l1-loss	0.10	0.17	0.10

707 **Table B.1: Reconstruction relative errors of the CNN (Lenhardt et al., 2024a) and the vision transformer models across**  
 708 **channels (CTH, COT and CWP) on the test dataset.**

$L_c$  and  $L_r$  for different tile sizes

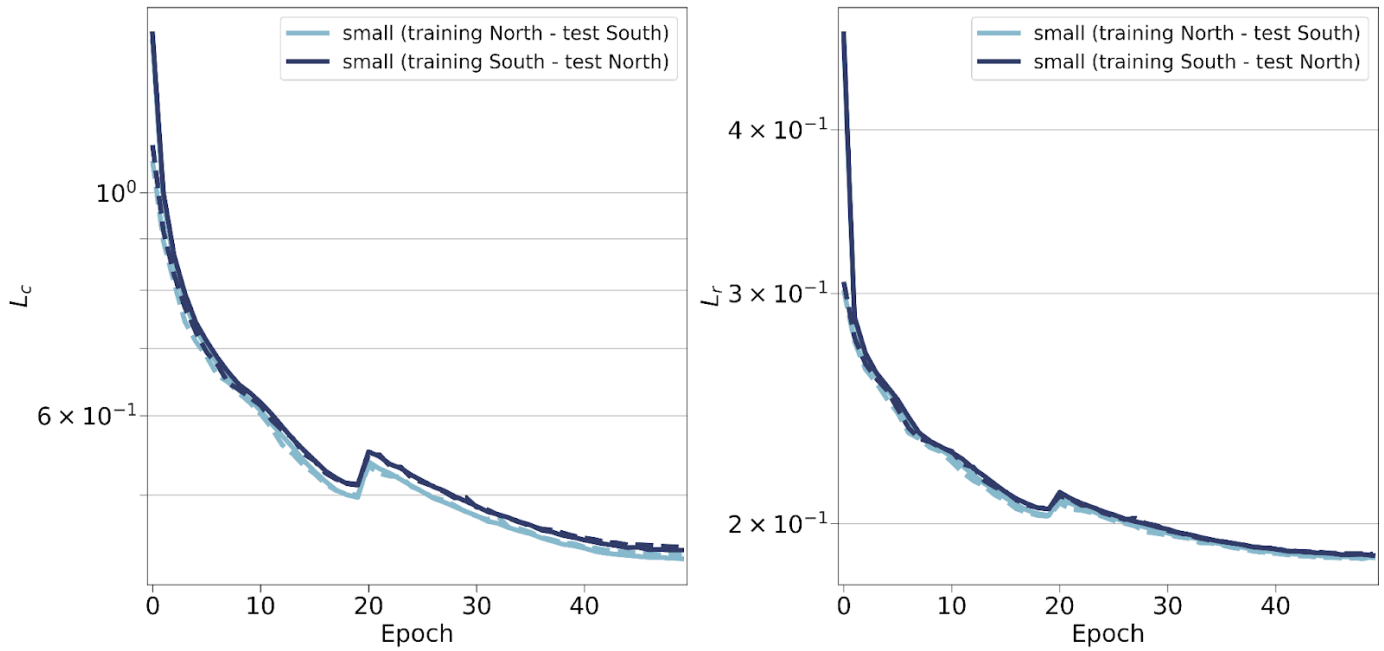


711  
 712 **Figure B.2: Training and validation contrastive (left) and reconstruction (right) losses for vision transformers trained on**  
 713 **different input tile sizes of 16, 32, 64 and 128.**  
 714



715  
 716 **Figure B.3: Input tiles (first and third rows) and corresponding reconstructions (second and fourth rows) for vision**  
 717 **transformers trained on the relevant input tile sizes of 16, 32, 64 and 128.**  
 718

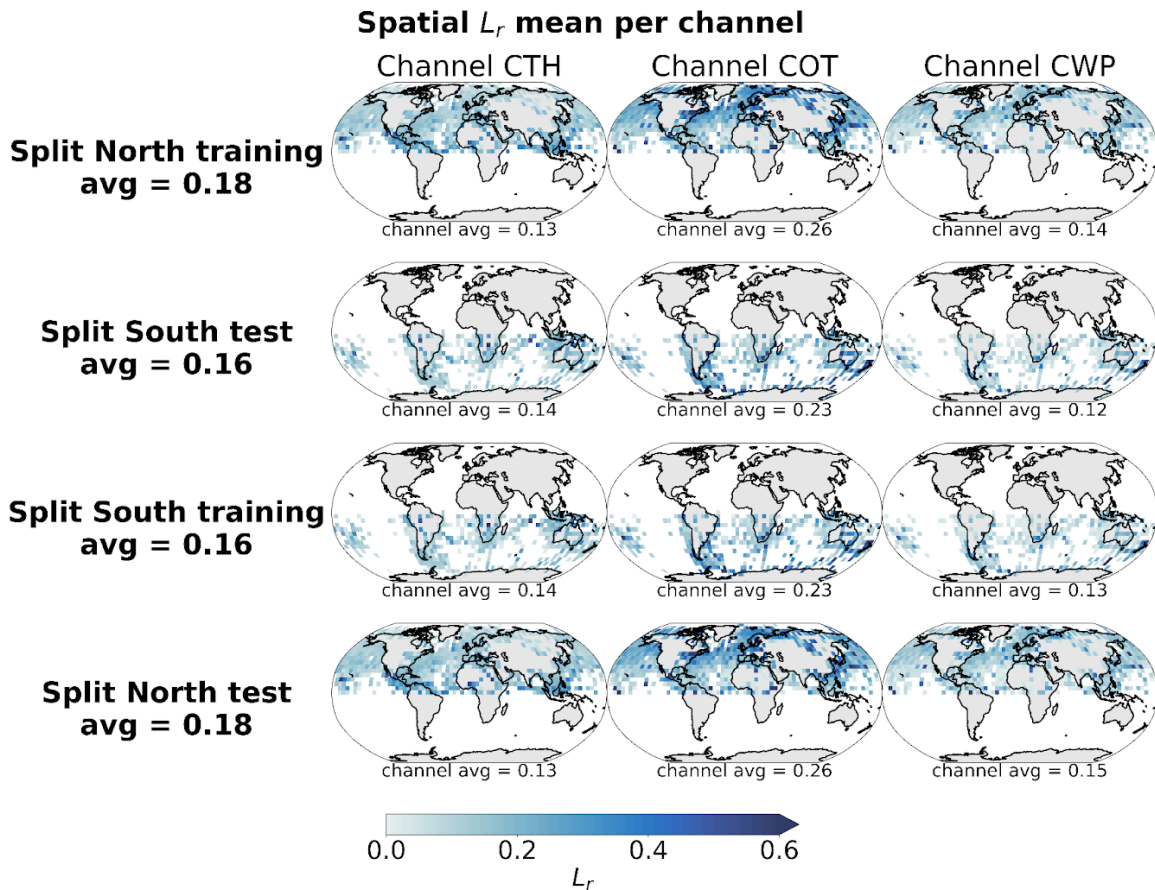
$L_c$  and  $L_r$  for different spatial splits



720

721 Figure B.4: Training (full lines) and validation (dashed lines) metrics for the contrastive (left) and reconstruction (right) losses for vision transformers trained on samples from the Northern or Southern hemispheres.

722



723

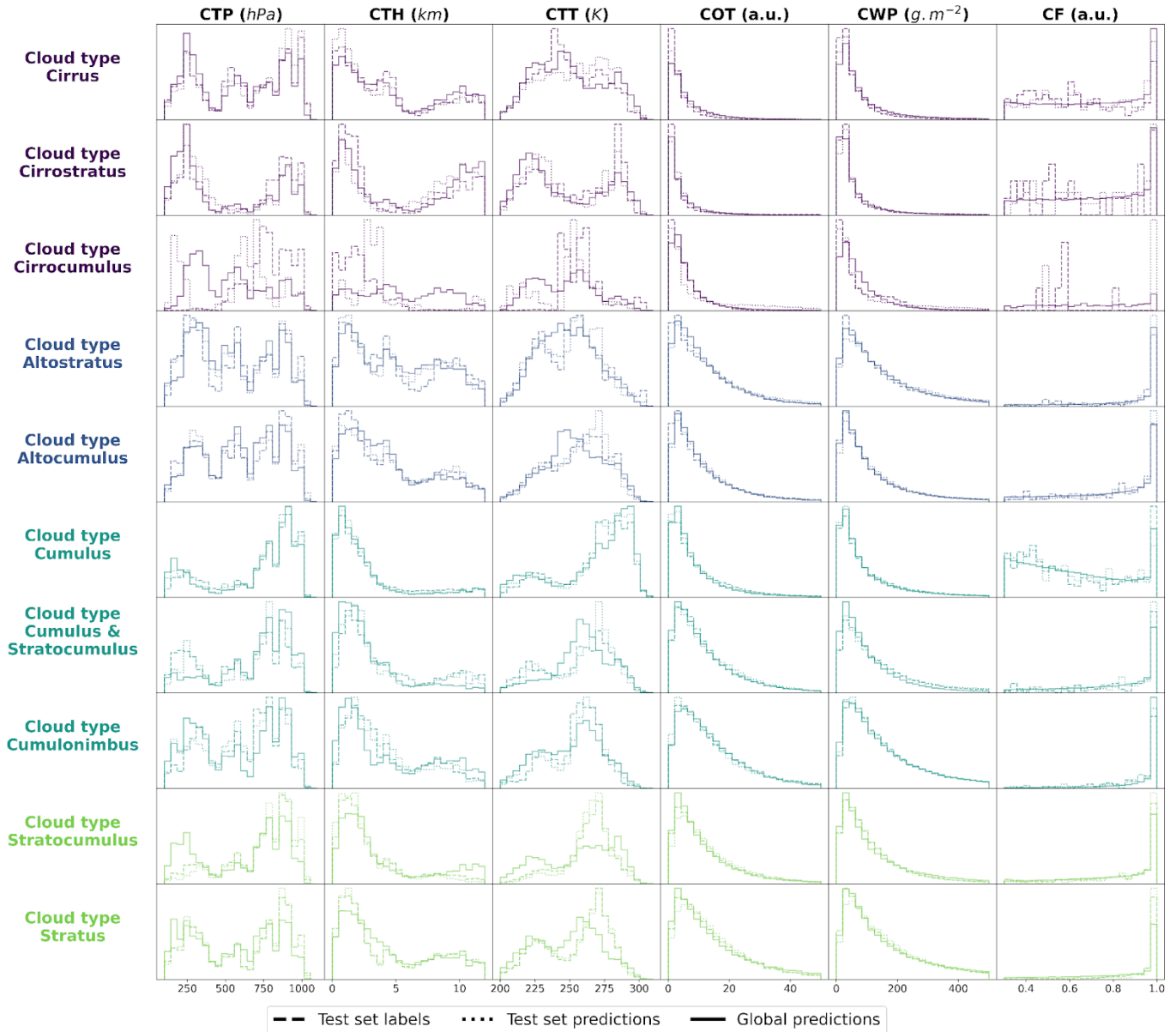
724 Figure B.5: Spatial distributions of the mean channel reconstruction errors for the Northern and Southern hemispheres  
725 colocated samples. The first two rows correspond to the model trained on the samples from the Northern hemisphere and  
726 the last two rows to the model trained on the samples from the Southern hemisphere.

727 Appendix C: Cloud type classification for 10 types

Method	Multi-class accuracy *	IBA geometric mean	F1-score *
Baseline 9x9 RF	0.19	0.26	0.16
Baseline CNN/RF	0.22	0.18	0.17
CloudViT/MLP	0.22	0.20	0.16
<b>CloudViT/RF</b>	<b>0.23</b>	<b>0.26</b>	<b>0.21</b>

728 Table C.1: Classification metrics on the test set in the case of 10 cloud types. The metrics noted with a \* are referring to  
 729 their macro-averaged estimate. The baseline CNN/RF refers to the CNN backbone introduced in Lenhardt et al. (2024a).  
 730

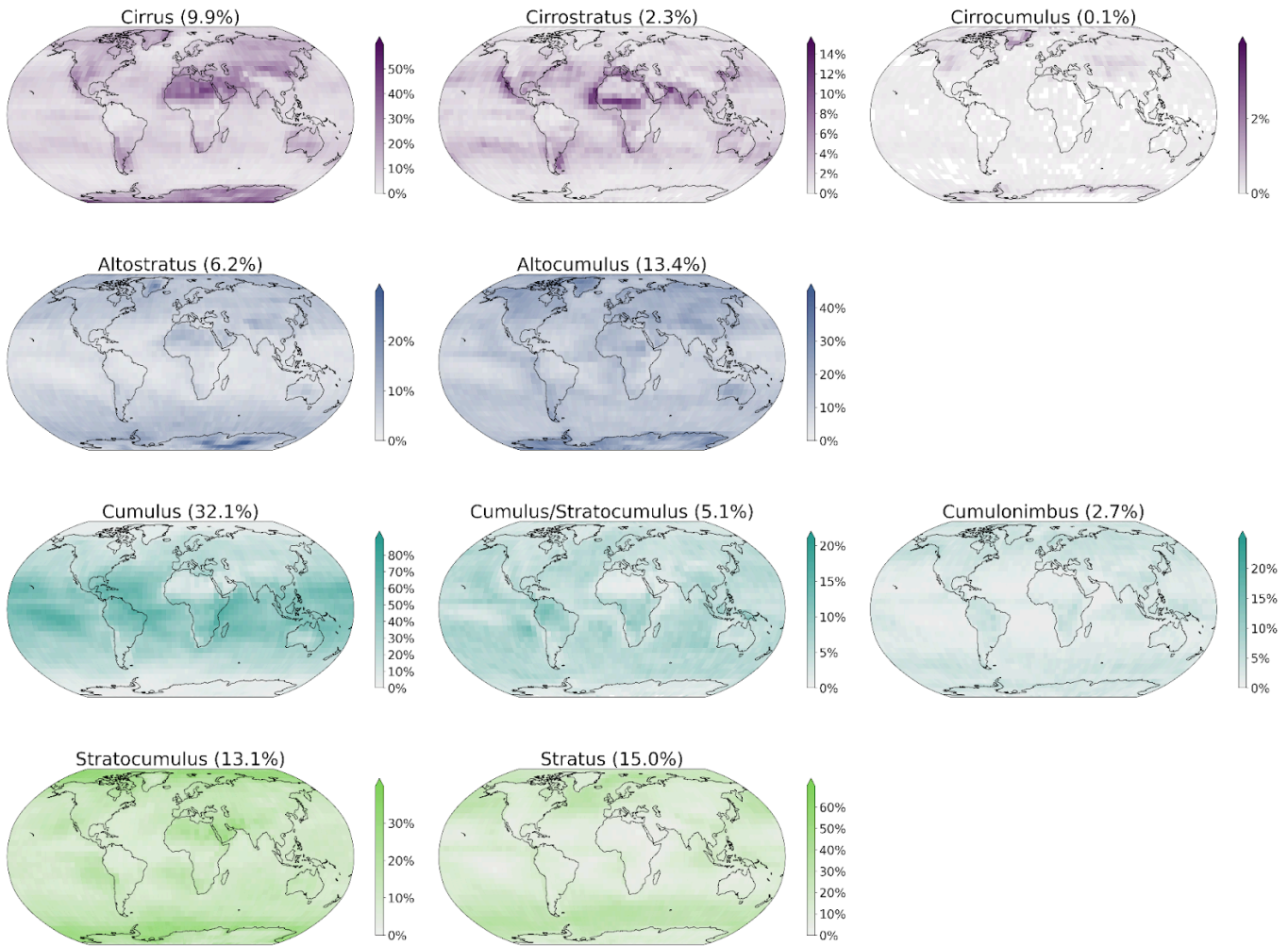
Density histograms of cloud properties per cloud class for test set labels, test set predictions and global predictions



731  
 732  
 733  
 734

Figure C.1: Density histograms of cloud properties for each cloud type from cirrus, cirrostratus, cirrocumulus, altostratus, alto cumulus, cumulus, cumulus and stratocumulus, cumulonimbus, stratocumulus, stratus.

### Spatial distributions of CloudViT cloud type occurrences (year 2016)



735

736 **Figure C.2: Spatial distributions of the CloudViT cloud type occurrences (cloud types cirrus, cirrostratus, cirrocumulus,**

737 **altostratus, alto cumulus, cumulus, cumulus and stratocumulus, cumulonimbus, stratocumulus, stratus) for MYD06**

738 **granules for the year 2016 aggregated on a 1° regular grid.**

## 739 Appendix D: Exploring the technical feasibility of the application to a global storm-resolving model simulation

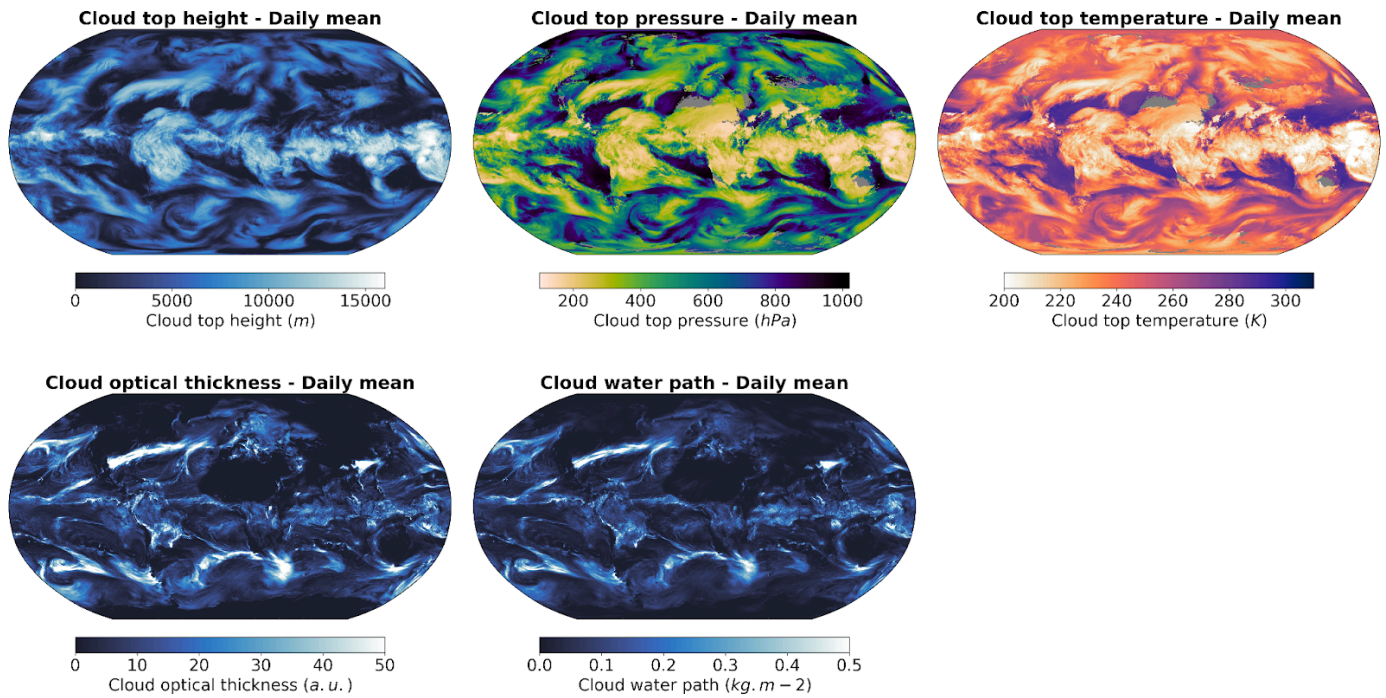
740

741 As a proof of concept and for probing the potential applicability of methods similar to CloudViT, we technically explore how to  
 742 investigate the cloud type representation in general circulation model (GCM) outputs. We build on a new generation of GCMs at  
 743 kilometre resolution, namely the ICON-Sapphire (Hohenegger et al., 2023). As the resolution of the simulation increases, some  
 744 processes like deep convection can be directly resolved instead of parameterized. Hence, building diagnostics about cloud  
 745 representation is of importance to help evaluate the simulations. In particular, we use the simulation run by the Max Planck  
 746 Institute for Meteorology (MPI-M) for the period between the 5th and 12th of December 1972, aiming at recreating the Blue  
 747 Marble picture made during the Apollo 17 mission on the 7th of December. Here we only use the complete outputs provided for  
 748 the 11th of December. The grid used contains 335 544 320 grid points at each level in the atmosphere (R02B11 grid), and outputs  
 749 are provided every 30 minutes during the simulation for the atmospheric quantities of interest, resulting in overall 48 time steps.  
 750 As the effective horizontal resolution of the model simulation and the MODIS data are on similar scales, we can technically  
 751 effectively apply CloudViT on the model outputs. From the model outputs, we derive the cloud properties necessary for the  
 752 method introduced in this study.

753 In order to compute the different cloud properties used in our method (Table 1), we use the available atmospheric outputs from  
 754 the model simulation. The simulation was made using the ICON-2.6.6-rc version in R02B11 grid resolution with 90 vertical  
 755 levels in the atmosphere (335544320 grid points per level) and 128 vertical levels in the ocean (237102291 surface grid points).  
 756 Observed aerosols and greenhouse gas concentrations of December 1972 were used for the atmosphere. The cloud top quantities  
 757 are retrieved by defining the top-most level where the liquid water content (variable name  $clw$ ) or the ice content (variable name  
 758  $cli$ ) are above a predefined threshold of  $1 \text{ mg.kg}^{-1}$ . This threshold relates to particles of sizes of at least a few micrometres which  
 759 is similar to what the sensors on the MODIS AQUA instrument are able to retrieve. Using 3D outputs of atmospheric quantities  
 760 like temperature (variable name  $ta$ ) and pressure (variable name  $pfull$ ), we derive the cloud top properties also present in the  
 761 MODIS MOD/MYD06 level 2 cloud properties product. The CTH is derived using the altitude in the corresponding vertical  
 762 level in the grid. Secondly, the CWP is computed by summing the vertically integrated cloud liquid water path (variable name  
 763  $cllvi$ ) and cloud ice path (variable name  $clivi$ ) which are already provided as simulation outputs. Lastly, we computed the COT by  
 764 vertically summing the layer-wise COT computed from the following equation, detailed in Carslaw (2022), equation 12.49  
 765 (Chapter 12.3, page 515):

$$766 \quad \tau_c = \frac{9}{5} \left(\frac{4\pi}{3\sqrt{2}}\right)^{1/3} \rho_w^{-2/3} (kN_d)^{1/3} c_w^{-1/6} L^{5/6} = 0.2303 \text{ kg}^{-5/6} \text{ m}^{8/3} (kN_d)^{1/3} L^{5/6} \quad (\text{D.1})$$

767 Where  $L = clw * \rho_{air} * \delta z$  the layer liquid water path,  $\rho_w = 1000 \text{ kg.m}^{-3}$  density of water,  $k = 1$  a factor to account for  
 768 the width of the droplet size distribution,  $c_w = 2e^{-6} \text{ kg.m}^{-4}$  the adiabatic condensation rate and  $N_d$  the vertical droplet number  
 769 defined in the simulation by the ECHAM6 parameterization (Equation 6; Stevens et al., 2013). However, the standardisation of  
 770 the input cloud properties for the vision transformer model is still done based on statistics computed on MODIS data which could  
 771 induce a bias in the latent representations and subsequently on the predictions. Extending the method to other datasets like this  
 772 GCM simulation thus requires careful investigation that the cloud properties lie in the same range or display similar distributions.  
 773 For each 30-minute time step, we proceed to sample tiles, regularly spaced, to reach global coverage of cloud type estimates.  
 774 Figure D.3 displays the daily averaged occurrence of the cloud type predictions on a  $1^\circ$  regular grid for the 4 cloud types, the  
 775 equivalent for 10 cloud types is presented in Figure D.4. However, due to the time period covered by the simulation, no global  
 776 data record for cloud types can be used to evaluate the representation of cloud types by the ICON-Sapphire through the  
 777 CloudViT method. A thorough analysis would be feasible for simulations covering a time period for which climate data records  
 778 of cloud types are available, for example the ISCCP H-series climate data record (Young et al., 2018) which starts in 1983. The  
 779 aim here is rather to present as a proof of concept the transfer of such a method to model data outputs. A large proportion of the  
 780 predicted clouds belong to the high cloud type, hinting at the difference in sensitivity to clouds retrieved in the climate model  
 781 data compared to the MODIS retrievals or the mismatch in the training process of CloudViT, high clouds being underrepresented  
 782 and their corresponding classification metrics lower than for some other cloud types. However, increasing the cloud ice content  
 783 threshold by an order of magnitude greatly decreases the amount of thin, high and cold clouds in the simulation dataset. This  
 784 aspect would need further tuning through comparison with remote sensing retrievals which are not available for this particular  
 785 simulated period. An important aspect to factor in is that the classification model was only trained on daytime satellite  
 786 observations as the optical cloud properties necessary are only available then. Thus, results on nighttime cloud retrievals which is  
 787 the case for some of the predictions produced from the presented simulation might need more meticulous evaluation. Even  
 788 though it is a limiting factor in the case of the satellite dataset we are using, the simulation outputs provide us with the required  
 789 variables across all timesteps.



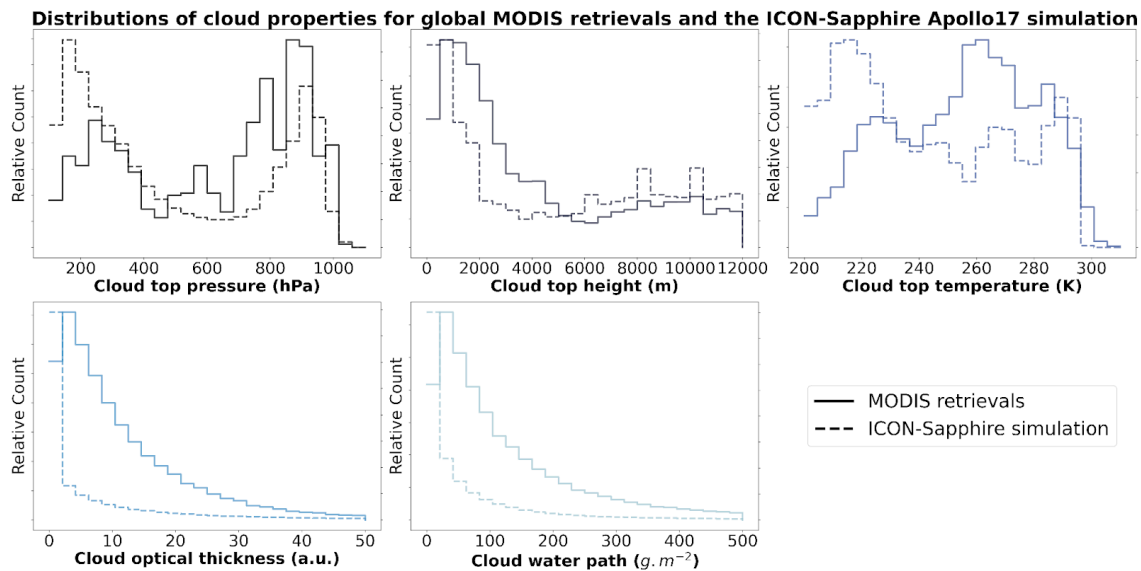
791

792

793

794

Figure D.1: Daily averages of cloud top height, cloud top pressure, cloud top temperature, cloud optical thickness and cloud water path for the 11th of December 1972 from the ICON-Sapphire Apollo 17 simulation.



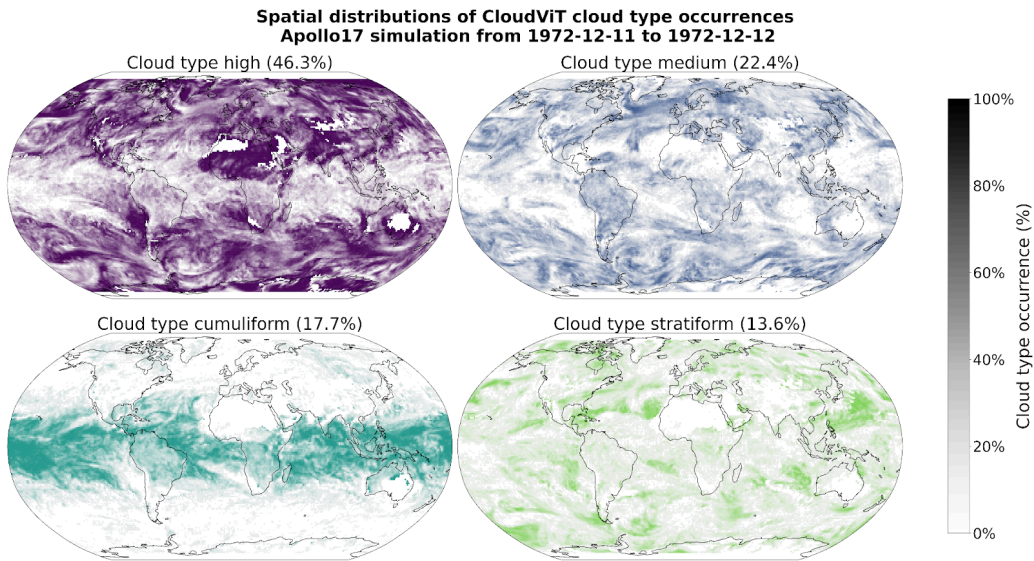
795

796

797

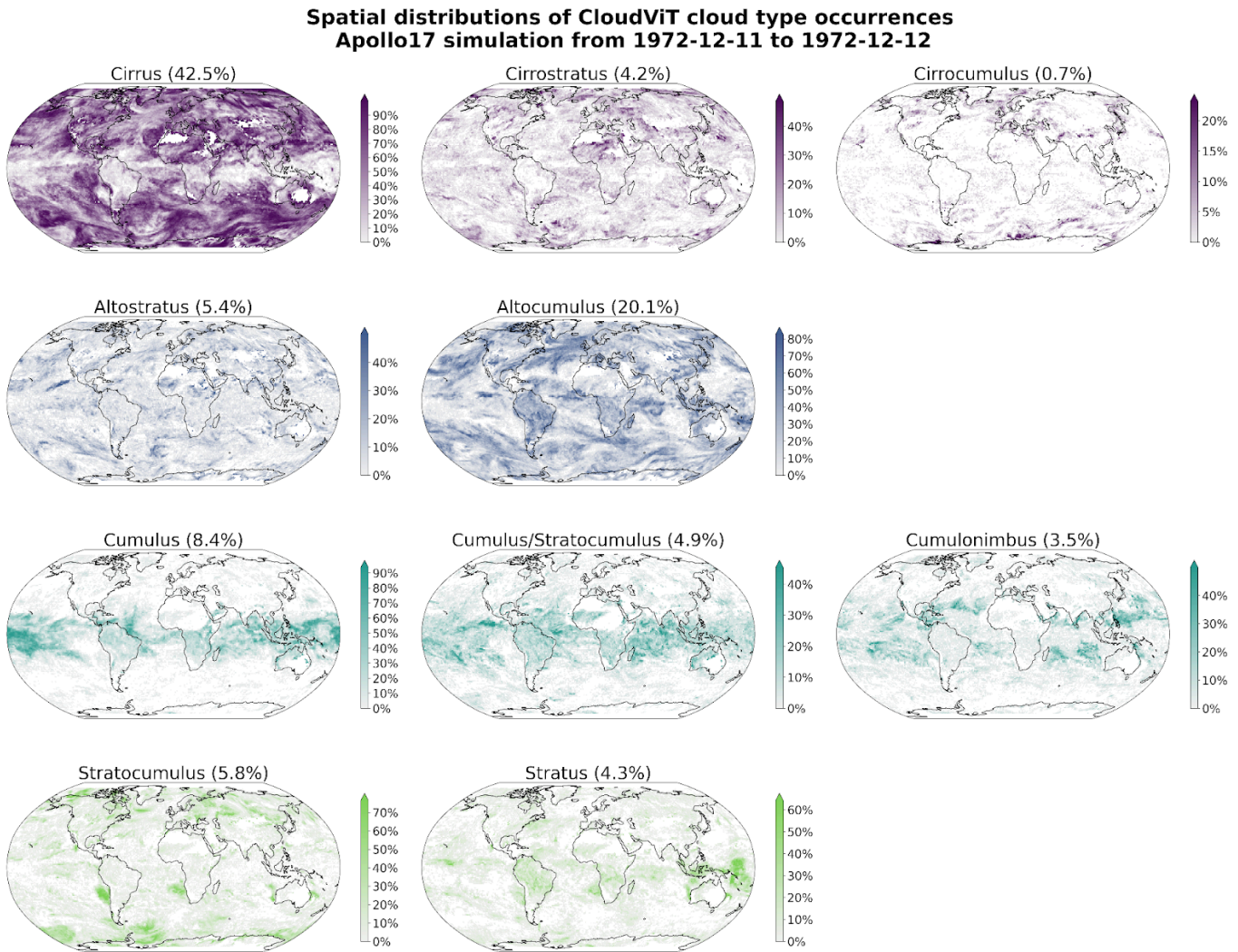
798

Figure D.2: Distribution of cloud top pressure, cloud top height, cloud top temperature, cloud optical thickness and cloud water path for MODIS AQUA retrievals and the ICON-Sapphire Apollo 17 simulation.



799  
800  
801

**Figure D.3: Spatial distributions of the CloudViT cloud type occurrences (cloud types high, medium, cumuliform, stratiform) for the ICON-Sapphire Apollo 17 simulation of December 11<sup>th</sup> 1972 aggregated on a 1° regular grid.**



802  
803  
804  
805

**Figure D.4: Spatial distribution of the CloudViT cloud type occurrences (cloud types cirrus, cirrostratus, cirrocumulus, altostratus, altostratus, altocumulus, cumulus, cumulus and stratocumulus, cumulonimbus, stratocumulus, stratus) for the ICON-Sapphire Apollo 17 simulation of December 11<sup>th</sup> 1972 aggregated on a 1° regular grid.**

## 806 Code availability

807  
808 The code used for the method and producing the plots is available on Zenodo (Lenhardt et al., 2024b).

## 809 Data availability

810  
811 The global dataset of the cloud type predictions for the year 2016 is available on Zenodo (Lenhardt et al., 2024b). The dataset is  
812 available as a csv file with corresponding coordinates, MODIS granule file, time of retrieval and predicted cloud type (4 and 10  
813 groups) or in a netCDF file as daily aggregates on a regular grid with a resolution of 1 ° or 5 °. The meteorological observations  
814 from the UK MetOffice (Met Office, 2006; Met Office 2008) are available through the CEDA archive at  
815 <https://catalogue.ceda.ac.uk/uuid/77910bcec71c820d4c92f40d3ed3f249> and  
816 <https://catalogue.ceda.ac.uk/uuid/9f80d42106ba708f92ada730ba321831> for ocean and land observations respectively. The files  
817 from the CUMULO dataset (Zantedeschi et al., 2019) are available at  
818 <https://www.dropbox.com/sh/i3s9q2v2jyjk2it/AACxXnXfMF5wuIqLXqH4NJOra?dl=0>. The simulation outputs are hosted by  
819 the DKRZ (Deutsches Klimarechenzentrum).

## 820 Author contribution

821  
822 JL, JQ, DS and DK designed the study. JL wrote the code. DK provided support regarding the climate model data. JL conducted  
823 the analysis and JL, JQ and DS interpreted the results. JL prepared the manuscript, JQ, DS and DK reviewed the manuscript and  
824 provided comments.

## 825 Competing interests

826  
827 Some authors are members of the editorial board of journal ACP.

## 828 Acknowledgements

829  
830 This work was supported by the European Union's Horizon 2020 research and innovation programme under Marie  
831 Skłodowska-Curie grant agreement No. 860100 (iMIRACLI). We thank the Leipzig University Scientific Computing cluster and  
832 the DKRZ (Deutsches Klimarechenzentrum, projects number bb1036 and bb1153) for computing and data hosting. We  
833 acknowledge the contributors of the CUMULO dataset (Zantedeschi et al., 2019) for providing access to the data files hosted at  
834 <https://www.dropbox.com/sh/i3s9q2v2jyjk2it/AACxXnXfMF5wuIqLXqH4NJOra?dl=0>. Additionally, we acknowledge the  
835 MODIS L2 Cloud product data set from the Level-1 and Atmosphere Archive and Distribution System (LAADS) Distributed  
836 Active Archive Center (DAAC), located in the Goddard Space Flight Center in Greenbelt, Maryland  
837 ([https://ladsweb.modaps.eosdis.nasa.gov/archive/allData/61/MYD06\\_L2/](https://ladsweb.modaps.eosdis.nasa.gov/archive/allData/61/MYD06_L2/)). We would like to also acknowledge Monika Esch,  
838 Emilie Fons and Hans Segura for support and discussions in handling the climate model data.

839

## 840 References

841

842 Ackerman, S. A., and Frey, R.: MODIS Atmosphere L2 Cloud Mask Product (35\_L2), NASA MODIS Adaptive Processing  
843 System, Goddard Space Flight Center, [http://doi.org/10.5067/MODIS/MOD35\\_L2.061](http://doi.org/10.5067/MODIS/MOD35_L2.061),  
844 [http://doi.org/10.5067/MODIS/MYD35\\_L2.061](http://doi.org/10.5067/MODIS/MYD35_L2.061), 2017.

845

846 Atito, S., Awais, M., & Kittler, J.: Sit: Self-supervised vision transformer, arXiv preprint,  
847 <https://doi.org/10.48550/arXiv.2104.03602>, 2021.

848

849 Baum, B.A., Menzel, W. P., Frey, R. A., Tobin, D. C., Holz, R. E., Ackerman, S. A., Heidinger, A. K., and Yang, P.: MODIS  
850 Cloud-Top Property Refinements for Collection 6, *Journal of Applied Meteorology and Climatology*, 51, 6, 1145-1163,  
851 <https://doi.org/10.1175/JAMC-D-11-0203.1>, 2012.

852

853 Bony, S., Semie, A., Kramer, R.J., Soden, B., Tompkins A.M., and Emanuel, K.A.: Observed modulation of the tropical radiation  
854 budget by deep convective organization and lower-tropospheric stability, *AGU Adv.*, Vol. 1, Issue 3,  
855 <https://doi.org/10.1029/2019av000155>, 2020.

856

857 Boucher, O., Randall, D., Artaxo, P., Bretherton, C., Feingold, G., Forster, P., Kerminen, V.-M., Kondo, Y., Liao, H., Lohmann,  
858 U., Rasch, P., Satheesh, S. K., Sherwood, S., Stevens, B. and Zhang, X. Y.: Clouds and aerosols, *Climate Change 2013: The*  
859 *Physical Science Basis. Contribution of Working Group I to the Fifth Assessment Report of the Intergovernmental Panel on*  
860 *Climate Change*, 571-657, <https://doi.org/10.1017/CBO9781107415324.016>, 2013.

861

862 Breiman, L.: Random Forests. *Machine Learning*, 45 (1), 5–32, <https://doi.org/10.1023/A:1010933404324>, 2001.

863

864 Carslaw, K.: *Aerosols and Climate*, 1st Edition, Elsevier, ISBN 9780128197660, 2022.

865

866 Cesana, G., Del Genio, A. D., and Chepfer, H.: The Cumulus And Stratocumulus CloudSat-CALIPSO Dataset (CASCCAD),  
867 *Earth Syst. Sci. Data*, 11, 1745–1764, <https://doi.org/10.5194/essd-11-1745-2019>, 2019.

868

869 Chawla, N. V., Bowyer, K. W., Hall, L. O., and Kegelmeyer, W. P.: Smote: synthetic minority over-sampling technique, *Journal*  
870 *of artificial intelligence research*, 16, 321–357, <https://doi.org/10.1613/jair.953>, 2002.

871

872 Chen, T., Kornblith, S., Norouzi, M., and Hinton, G.: A simple framework for contrastive learning of visual representations, in:  
873 *Proceedings of the 37th International Conference on Machine Learning (ICML'20)*, *Journal of Machine Learning Research*, 119,  
874 1597–1607, <https://dl.acm.org/doi/10.5555/3524938.3525087>, 2020.

875

876 Deng, J., Dong, W., Socher, R., Li, L., Li, K., and Fei-Fei, L.: Imagenet: A large-scale hierarchical image database, in: 2009  
877 *IEEE conference on computer vision and pattern recognition*, Miami, FL, USA, 248–255,  
878 <https://doi.org/10.1109/CVPR.2009.5206848>, 2009.

879

880 Dhuria, H. L. and Kyle, H. L.: Cloud Types and the Tropical Earth Radiation Budget, *J. Clim.*, 3, 1409–1434,  
881 [https://doi.org/10.1175/1520-0442\(1990\)003<1409:CTATTE>2.0.CO;2](https://doi.org/10.1175/1520-0442(1990)003<1409:CTATTE>2.0.CO;2), 1990.

882

883 Dosovitskiy, A., Beyer, L., Kolesnikov, A., Weissenborn, D., Zhai, X., Unterthiner, T., Dehghani, M., Minderer, M., Heigold, G.,  
884 Gelly, S., Uszkoreit, J., and Houlsby, N. : An image is worth 16x16 words: Transformers for image recognition at scale, arXiv  
885 preprint, <https://doi.org/10.48550/arXiv.2010.11929>, 2020.

886

887 Forster, P., T. Storelvmo, K. Armour, W. Collins, J.-L. Dufresne, D. Frame, D.J. Lunt, T. Mauritsen, M.D. Palmer, M. Watanabe,  
888 M. Wild, and H. Zhang: The Earth's Energy Budget, Climate Feedbacks, and Climate Sensitivity, in *Climate Change 2021: The*  
889 *Physical Science Basis. Contribution of Working Group I to the Sixth Assessment Report of the Intergovernmental Panel on*  
890 *Climate Change* [Masson-Delmotte, V., P. Zhai, A. Pirani, S.L. Connors, C. Péan, S. Berger, N. Caud, Y. Chen, L. Goldfarb, M.I.  
891 Gomis, M. Huang, K. Leitzell, E. Lonnoy, J.B.R. Matthews, T.K. Maycock, T. Waterfield, O. Yelekçi, R. Yu, and B. Zhou (eds.)].

892 Cambridge University Press, Cambridge, United Kingdom and New York, NY, USA, pp. 923–1054,  
893 <http://doi.org/10.1017/9781009157896.009>, 2021.  
894

895 García, V., Sánchez, J. S., and Mollineda, R. A.: On the effectiveness of preprocessing methods when dealing with different  
896 levels of class imbalance, *Knowledge-Based Systems*, 25, 13–21, <https://doi.org/10.1016/j.knosys.2011.06.013>, 2012.  
897

898 Hartmann, D. L., Ockert-Bell, M. E., and Michelsen, M. L.: The Effect of Cloud Type on Earth's Energy Balance: Global  
899 Analysis, *J. Clim.*, 5, 1281–1304, [https://doi.org/10.1175/1520-0442\(1992\)005<1281:TEOCTO>2.0.CO;2](https://doi.org/10.1175/1520-0442(1992)005<1281:TEOCTO>2.0.CO;2), 1992.  
900

901 Hendrycks, D., and Gimpel, K.: Gaussian error linear units (gelus), arXiv preprint, <https://doi.org/10.48550/arXiv.1606.08415>,  
902 2016.  
903

904 Hinton, G. E.: Connectionist learning procedures, *Artificial intelligence*, 40, 185-234,  
905 [https://doi.org/10.1016/0004-3702\(89\)90049-0](https://doi.org/10.1016/0004-3702(89)90049-0), 1989.  
906

907 Hohenegger, C., Korn, P., Linardakis, L., Redler, R., Schnur, R., Adamidis, P., Bao, J., Bastin, S., Behraves, M., Bergemann,  
908 M., Biercamp, J., Bockelmann, H., Brokopf, R., Brüggemann, N., Casaroli, L., Chegini, F., Datseris, G., Esch, M., George, G.,  
909 Giorgetta, M., Gutjahr, O., Haak, H., Hanke, M., Ilyina, T., Jahns, T., Jungclaus, J., Kern, M., Klocke, D., Kluft, L., Kölling, T.,  
910 Kornblueh, L., Kosukhin, S., Kroll, C., Lee, J., Mauritsen, T., Mehlmann, C., Mieslinger, T., Naumann, A. K., Paccini, L.,  
911 Peinado, A., Praturi, D. S., Putrasahan, D., Rast, S., Riddick, T., Roeber, N., Schmidt, H., Schulzweida, U., Schütte, F., Segura,  
912 H., Shevchenko, R., Singh, V., Specht, M., Stephan, C. C., von Storch, J.-S., Vogel, R., Wengel, C., Winkler, M., Ziemer, F.,  
913 Marotzke, J., and Stevens, B.: ICON-Sapphire: simulating the components of the Earth system and their interactions at kilometer  
914 and subkilometer scales, *Geosci. Model Dev.*, 16, 779–811, <https://doi.org/10.5194/gmd-16-779-2023>, 2023.  
915

916 Howard, L.: *Essay on the modifications of clouds*, John Churchill & Sons, London, 64 pp., 1803.  
917

918 Kaps, A., Lauer, A., Camps-Valls, G., Gentine, P., Gómez-Chova, L., and Eyring, V.: Machine-Learned Cloud Classes From  
919 Satellite Data for Process-Oriented Climate Model Evaluation, *IEEE Transactions on Geoscience and Remote Sensing*, 61, 1-15,  
920 4100515, <https://doi.org/10.1109/TGRS.2023.3237008>, 2023.  
921

922 Kuma, P., Bender, F. A.-M., Schuddeboom, A., McDonald, A. J., and Seland, Ø.: Machine learning of cloud types in satellite  
923 observations and climate models, *Atmos. Chem. Phys.*, 23, 523–549, <https://doi.org/10.5194/acp-23-523-2023>, 2023.  
924

925 Kurihana, T., Moyer, E., Willett, R., Gilton, D.y, and Foster, I.: Data-Driven Cloud Clustering via a Rotationally Invariant  
926 Autoencoder, *IEEE Transactions on Geoscience and Remote Sensing*, 60, 1-25, 4103325,  
927 <https://doi.org/10.1109/TGRS.2021.3098008>, 2022.  
928

929 LeCun, Y., Jackel, L. D., Boser, B., Denker, J. S., Graf, H. P., Guyon, I., Henderson, D., Howard, R. E., and Hubbard, W.:  
930 Handwritten digit recognition: Applications of neural network chips and automatic learning, *IEEE Communications Magazine*,  
931 Volume 27, Issue 11, 41-46, <https://doi.org/10.1109/35.41400>, 1989.  
932

933 LeCun, Y., and Bengio, Y.: Convolutional networks for images, speech, and time series, *The handbook of brain theory and neural*  
934 *networks*, 3361, 10, 1995.  
935

936 Lemaitre, G., Nogueira, F., and Aridas, C., K.: Imbalanced-learn: A Python Toolbox to Tackle the Curse of Imbalanced Datasets  
937 in Machine Learning, *Journal of Machine Learning Research*, 18, 1-5, <http://jmlr.org/papers/v18/16-365.html>, 2017.  
938

939 Luo, H., Quaas, J., and Han, Y.: Examining cloud vertical structure and radiative effects from satellite retrievals and evaluation of  
940 CMIP6 scenarios, *Atmos. Chem. Phys.*, 23, 8169–8186, <https://doi.org/10.5194/acp-23-8169-2023>, 2023.  
941

942 Luo, H., Quaas, J., and Han, J.: Diurnally asymmetric cloud cover trends amplify greenhouse warming, *Science Advances*, 10,  
943 25, <https://doi.org/10.1126/sciadv.ado5179>, 2024.

944

945 Lenhardt, J., Quaas, J., and Sejdinovic, D.: Marine cloud base height retrieval from MODIS cloud properties using machine  
946 learning, *Atmos. Meas. Tech.*, 17, 5655–5677, <https://doi.org/10.5194/amt-17-5655-2024>, 2024a.

947

948 Lenhardt, J., Quaas, J., Sejdinovic, D., and Klocke, D.: CloudViT - Method code and data for the article "CloudViT: classifying  
949 cloud types in global satellite data and in kilometre-resolution simulations using vision transformers.", Zenodo,  
950 <https://doi.org/10.5281/zenodo.12731288>, 2024b.

951

952 McCoy, I. L., McCoy, D. T., Wood, R., Zuidema, P., and Bender, F. A. M.: The role of mesoscale cloud morphology in the  
953 shortwave cloud feedback, *GRL*, 50, 2, <https://doi.org/10.1029/2022gl101042>, 2023.

954

955 Met Office: LAND SYNOP reports from land stations collected by the Met Office MetDB System, NCAS British Atmospheric  
956 Data Centre, <https://catalogue.ceda.ac.uk/uuid/9f80d42106ba708f92ada730ba321831>, 2008.

957

958 Met Office: MIDAS: Global Marine Meteorological Observations Data, NCAS British Atmospheric Data Centre,  
959 <https://catalogue.ceda.ac.uk/uuid/77910bcec71c820d4c92f40d3ed3f249>, 2006.

960

961 Muhlbauer, A., McCoy, I. L., and Wood, R.: Climatology of stratocumulus cloud morphologies: microphysical properties and  
962 radiative effects, *Atmos. Chem. Phys.*, 14, 6695–6716, <https://doi.org/10.5194/acp-14-6695-2014>, 2014.

963

964 Oreopoulos, L., Cho, N., and Lee, D.: New insights about cloud vertical structure from CloudSat and CALIPSO observations, *J.*  
965 *Geophys. Res.-Atmos.*, 122, 9280–9300, <https://doi.org/10.1002/2017JD026629>, 2017.

966

967 Paszke, A., Gross, S., Massa, F., Lerer, A., Bradbury, J., Chanan, G., Killeen, T., Lin, Z., Gimelshein, N., Antiga, L., Desmaison,  
968 A., Kopf, A., Yang, E., DeVito, Z., Raison, M., Tejani, A., Chilamkurthy, S., Steiner, B., Fang, L., Bai, J. and Chintala, S.:  
969 PyTorch: An Imperative Style, High-Performance Deep Learning Library, in *Advances in Neural Information Processing*  
970 *Systems* 32 (NeurIPS), 8024–8035,  
971 <http://papers.neurips.cc/paper/9015-pytorch-an-imperative-style-high-performance-deep-learning-library.pdf>, 2019.

972

973 Pedregosa, F., Varoquaux, G., Gramfort, A., Michel, V., Thirion, B., Grisel, O., Blondel, M., Prettenhofer, P., Weiss, R., Dubourg,  
974 V., Vanderplas, J., Passos, A., Cournapeau, D., Brucher, M., Perrot, M., and Duchesnay, E.: Scikit-learn: Machine Learning in  
975 Python, *Journal of Machine Learning Research*, 12, 2825–2830, <https://www.jmlr.org/papers/v12/pedregosa11a.html>, 2011.

976

977 Pincus, R., Hubanks, P. A., Platnick, S., Meyer, K., Holz, R. E., Botambekov, D., and Wall, C. J.: Updated observations of clouds  
978 by MODIS for global model assessment, *Earth Syst. Sci. Data*, 15, 2483–2497, <https://doi.org/10.5194/essd-15-2483-2023>, 2023.

979

980 Platnick, S., Ackerman, S. A., King, M. D., Meyer, K., Menzel, W. P., Holz, R. E., Baum, B. A., and Yang, P.: MODIS  
981 atmosphere L2 cloud product (06\_L2), NASA MODIS Adaptive Processing System, Goddard Space Flight Center,  
982 [http://doi.org/10.5067/MODIS/MYD06\\_L2.061](http://doi.org/10.5067/MODIS/MYD06_L2.061), 2017.

983

984 Platnick, S., King, M.D., Ackerman, S.A., Menzel, W.P., Baum, B.A., Riedi, J.C., and Frey, R.A.: The MODIS cloud products:  
985 algorithms and examples from Terra, in: *IEEE Transactions on Geoscience and Remote Sensing*, Volume 41, Number 2, 459–473,  
986 <http://doi.org/10.1109/TGRS.2002.808301>, 2003.

987

988 Ramanathan, V., Cess, R. D., Harrison, E. F., Minnis, P., Barkstrom, B. R., Ahmad, E., and Hartmann, D.: Cloud Radiative  
989 Forcing and Climate: Results from the Earth Radiation Budget Experiment, *Science*, 243, 57–63,  
990 <https://doi.org/10.1126/science.243.4887.57>, 1989.

991

992 Rasp, S., Schulz, H., Bony, S., and Stevens, B.: Combining Crowdsourcing and Deep Learning to Explore the Mesoscale  
993 Organization of Shallow Convection, *Bulletin of the American Meteorological Society*, 101, E1980–E1995,  
994 <https://doi.org/10.1175/BAMS-D-19-0324.1>, 2020.

995

996 Ronneberger, O., Fischer, P., and Brox, T.: U-Net: Convolutional Networks for Biomedical Image Segmentation, in: Navab, N.,  
997 Hornegger, J., Wells, W., Frangi, A. (eds) Medical Image Computing and Computer-Assisted Intervention (MICCAI 2015),  
998 Lecture Notes in Computer Science, Volume 9351, Springer, Cham., [https://doi.org/10.1007/978-3-319-24574-4\\_28](https://doi.org/10.1007/978-3-319-24574-4_28), 2015.  
999

1000 Rossow, W.B., and Schiffer, R.A.: ISCCP cloud data products, *Bull. Amer. Meteorol. Soc.*, 71, 2-20, 1991.  
1001

1002 Sassen, K., Wang, Z., and Liu, D.: Global distribution of cirrus clouds from CloudSat/Cloud-Aerosol Lidar and Infrared  
1003 Pathfinder Satellite Observations (CALIPSO) measurements, *J. Geophys. Res.*, Volume 113, D00A12,  
1004 <https://doi.org/10.1029/2008JD009972>, 2008.  
1005

1006 Slingo, A.: Sensitivity of the Earth's radiation budget to changes in low clouds, *Nature*, 343, 49–51  
1007 <https://doi.org/10.1038/343049a0>, 1990.  
1008

1009 Stevens, B., Giorgetta, M., Esch, M., Mauritsen, T., Crueger, T., Rast, S., Salzmann, M., Schmidt, H., Bader, J., Block, K.,  
1010 Brokopf, R., Fast, I., Kinne, S., Kornblueh, L., Lohmann, U., Pincus, R., Reichler, T., and Roeckner, E.: Atmospheric component  
1011 of the MPI-M Earth System Model: ECHAM6, *Journal of Advances in Modeling Earth Systems*, 5, 2, 146-172,  
1012 <https://doi.org/10.1002/jame.20015>, 2013.  
1013

1014 Stevens, B., Bony, S., Brogniez, H., Hentgen, L., Hohenegger, C., Kiemle, C., L'Ecuyer, T. S., Naumann, A. K., Schulz, H.,  
1015 Siebesma, P. A., Vial, J., Winker, D. M., and Zuidema, P.: Sugar, gravel, fish and flowers: Mesoscale cloud patterns in the trade  
1016 winds, *Q. J. R. Meteorol. Soc.*, Vol. 146, Issue 726, <https://doi.org/10.1002/qj.3662>, 2020.  
1017

1018 Touvron, H., Vedaldi, A., Douze, M., and Jegou, H.: Fixing the train-test resolution discrepancy, 33rd Conference on Neural  
1019 Information Processing Systems (NeurIPS 2019), Vancouver, Canada, <https://doi.org/10.48550/arXiv.1906.06423>, 2019.  
1020

1021 Tzallas, V., Hünerbein, A., Stengel, M., Meirink, J. F., Benas, N., Trentmann, J., Macke, A.: CRAAS: A European Cloud Regime  
1022 dAtASET Based on the CLAAS-2.1 Climate Data Record, *Remote Sensing*, 14, 5548, <https://doi.org/10.3390/rs14215548>, 2022.  
1023

1024 Unglaub, C., Block, K., Mülmenstädt, J., Sourdeval, O., and Quaas, J.: A new classification of satellite-derived liquid water  
1025 cloud regimes at cloud scale, *Atmos. Chem. Phys.*, 20, 2407–2418, <https://doi.org/10.5194/acp-20-2407-2020>, 2020.  
1026

1027 Vaswani, A., Shazeer, N., Parmar, N., Uszkoreit, J., Jones, L., Gomez, A.N., Kaiser, L., and Polosukhin, I.: Attention Is All You  
1028 Need, arXiv preprint, <https://doi.org/10.48550/ARXIV.1706.03762>, 2017.  
1029

1030 WMO: Manual on the observation of clouds and other meteors - International Cloud Atlas Volume I (WMO-No. 407), available  
1031 at: [https://cloudatlas.wmo.int/docs/wmo\\_407\\_en-v1.pdf](https://cloudatlas.wmo.int/docs/wmo_407_en-v1.pdf) (last access: 25 February 2025), 1975.  
1032

1033 WMO: Manual on the observation of clouds and other meteors - International Cloud Atlas (WMO-No. 407), available at:  
1034 <https://cloudatlas.wmo.int> (last access: 25 February 2025), 2017.  
1035

1036 WMO: Manual on Codes, Volume I.1 – International Codes, Annex II to the WMO Technical Regulations, Part A –  
1037 Alphanumeric Codes (WMO-No. 306), ISBN: 978-92-63-10306-2, available at: <https://library.wmo.int/idurl/4/35713>, 2019.  
1038

1039 Wood, R.: Stratocumulus clouds, *Monthly Weather Review*, 140, 8, 2373–2423, <https://doi.org/10.1175/MWR-D-11-00121.1>,  
1040 2012.  
1041

1042 Wood, R., and Hartmann, D. L.: Spatial variability of Liquid water path in marine low cloud: The importance of mesoscale  
1043 cellular convection, *J Clim*, 19, 9, 1748–1764, <https://doi.org/10.1175/jcli3702.1>, 2006.  
1044

1045 Young, A. H., Knapp, K. R., Inamdar, A., Hankins, W., and Rossow, W. B.: The International Satellite Cloud Climatology  
1046 Project H-Series climate data record product, *Earth Syst. Sci. Data*, 10, 583–593, <https://doi.org/10.5194/essd-10-583-2018>,  
1047 2018.

1048

1049 Yuan, T., Song, H., Wood, R., Mohrmann, J., Meyer, K., Oreopoulos, L., and Platnick, S.: Applying deep learning to NASA  
1050 MODIS data to create a community record of marine low-cloud mesoscale morphology, *Atmos. Meas. Tech.*, 13, 6989–6997,  
1051 <https://doi.org/10.5194/amt-13-6989-2020>, 2020.

1052

1053 Zantedeschi, V., Falasca, F., Douglas, A., Strange, R., Kusner, M. J., and Watson-Parris, D.: Cumulo: A Dataset for Learning  
1054 Cloud Classes, *Tackling Climate Change with Machine Learning Workshop*, 33rd Conference on Neural Information Processing  
1055 Systems (NeurIPS 2019), Vancouver, Canada, <https://doi.org/10.48550/arXiv.1911.04227>, 2019.

1056

1057 Zhang, J. L., Liu, P., Zhang, F., & Song, Q. Q.: CloudNet: Ground-based cloud classification with deep convolutional neural  
1058 network, *Geophysical Research Letters*, 45, 8665–8672, <https://doi.org/10.1029/2018GL077787>, 2018.

1059

1060 Zhao, H., Gallo, O., Frosio, I., and Kautz, J.: Loss functions for image restoration with neural networks, *IEEE Transactions on*  
1061 *computational imaging*, 3, 1, 47–57, <https://doi.org/10.1109/TCI.2016.2644865>, 2016.